Characterization of Pro-Fibrotic Signaling Pathways using Human Hepatic Organoids

Yuan Guan, Zhuoqing Fang, Angelina Hu, Sarah Roberts, Patrik K. Johansson[1], Sarah C. Heilshorn[1], Annika Enejder[1] and Gary Peltz[*]

Department of Anesthesia, Pain and Perioperative Medicine, Stanford University School of Medicine, Stanford CA, 94305; and [1]Department of Materials Science and Engineering, Stanford University, Stanford CA, 94305

Financial support: Y.G. and G.P. were supported by awards from the NIDDK (1R56DK12930901A1). P.K.J., S.C.H., and A.E were supported by awards from the National Science Foundation (CBET 2033302).

The authors have declared that no conflict of interest exists.

*Address Correspondence to: gpeltz@stanford.edu 300 Pasteur Dr. Room L232 Stanford, CA 94305.

Abstract

Due to the limitations of available *in vitro* systems and animal models, we lack a detailed understanding of the pathogenetic mechanisms and have minimal treatment options for liver fibrosis. To overcome this barrier, we engineered a live cell imaging system that identifies collagen producing cells in a human multi-lineage hepatic organoid. This system was adapted for use as a microwell-based platform (i.e., microHOs) where exposure to PDGF or TGFβ1 induced the formation of thick collagen fibers. Transcriptomic analysis revealed that TGFβ1 exposure converted mesenchymal cells into myofibroblast-like cells with a significantly altered pattern of production of proteases and anti-proteases, which contribute to the development of liver fibrosis. When pro-fibrotic intracellular signaling pathways were examined using pharmacological probes, the anti-fibrotic effect of receptor-specific tyrosine kinase inhibitors was limited to the fibrosis induced by the corresponding growth factor, which indicates that their anti-fibrotic efficacy would be limited to fibrotic diseases that were solely mediated by that growth factor. In contrast, GSK3β or p38 MAPK inhibitors could prevent TGFβ1- or PDGF-induced fibrosis in microHOs because they block intracellular signaling pathways that are commonly utilized by the TGFβ1 and PDGF receptors. Hence, these studies identified GSK3β and p38 MAPK inhibitors as potential new broad-spectrum therapies for liver fibrosis, and it is likely that other new therapies could subsequently be identified using this microHO system.

Word count: 220

Abbreviations: ARPKD, Autosomal Recessive Polycystic Kidney Disease; ECM, extra-cellular matrix; HCS, high content screening; HO, hepatic organoid; HSC, hepatic stellate cells; iPSC, induced pluripotent stem cells; MAPK, Mitogen Activated Protein Kinase; NASH, non-alcoholic steatohepatitis; SHG, Second Harmonic Generation.

Liver fibrosis is a pathological condition caused by the accumulation of extracellular matrix (**ECM**) that develops in response to chronic liver injury [1,2]. It results from an interaction between parenchymal and nonparenchymal liver cells and involves endogenous and liver infiltrating immune cells [3-5]. The key non-parenchymal cell is the myofibroblast, which is generated when a fibrogenic stimulus induced by liver injury causes hepatic stellate cells (**HSC**) to transdifferentiate into myofibroblasts that produce fibril-forming collagens and other ECM components [5-9]. Before organoid methodology was available, *in vitro* models often did not have the spectrum of cell types that mediate fibrogenesis, which limited our ability to explore fibrogenic mechanisms. Commonly used rodent models require an injury inducing agent (carbon tetrachloride, bile duct ligation, or dietary modulation); are very time consuming and expensive to run; and any conclusions drawn from them are limited by concerns about their fidelity with the processes mediating the commonly occurring forms of human liver fibrosis [10]. However, the pathogenesis of liver fibrosis can best be studied using a multi-lineage human hepatic organoid (**HO**) that has the cellular components and the geometry of hepatic lobules, which enables the effect that biochemical signals have on fibrosis to be quantitatively characterized. We previously developed an *in vitro* model system that differentiates human induced pluripotent stem cells (**iPSCs**) into a multi-lineage HO that has hepatocytes, cholangiocytes, HSCs, and cells of other lineages (fibroblasts, macrophages, and endothelial cells); and bile ducts and other structures found in the liver lobule are formed in these HOs [11,12]. HOs engineered to express a causative mutation for Autosomal Recessive Polycystic Kidney Disease (**ARPKD**) developed an extensive fibrosis [12] that was characterized by a marked increase in thick collagen fiber formation, which resembled that in liver tissue obtained from ARPKD patients. The myofibroblasts in ARPKD organoids resembled those in the livers of patients with viral-induced cirrhosis or advanced non-alcoholic steatohepatitis (**NASH**) [12]. Here, we engineered a live cell imaging system for identification of the collagen producing cells in hepatic organoids that was adapted for use in a microwell-based platform. This system was used to characterize the signals driving liver fibrosis at the whole organoid, single cell, and molecular levels. Moreover, when the interaction between the intracellular signaling pathways activated by two pro-fibrotic factors were characterized using pharmacological agents, two potential new approaches for treating liver fibrosis were identified.

Results

A live cell imaging system for hepatic fibrosis. Collagen is a triple helical protein that is composed of two COL1A1 (α1) and one COL1A2 (α2) chains, and increased collagen synthesis

by activated myofibroblasts is a major contributor to liver fibrosis [2]. To characterize fibrogenic mechanisms, we developed a live cell imaging system, which enabled collagen producing cells in HOs to be identified and quantitatively analyzed. A CRISPR-assisted insertion tagging system (CRISPaint) [13] was used to insert a Clover expression cassette (***COL1A1*-P2A Clover**) at the COOH terminus of the endogenous *COL1A1* gene in an iPSC line. Since the insert has a self-cleaving P2A peptide, *COL1A1* mRNA expressing cells in HOs produced from *COL1A1*-P2A Clover iPSCs were labelled with a fluorescent intracellular protein (**Fig 1A-B**). The Clover$^+$ cell population gradually increased when HO cultures were differentiated beyond the hepatoblast stage (day 9) (**Fig. 1C**) and was markedly increased in day 21 HOs that were treated with TGFβ1 or PDGFβ on day 13 (**Fig. 1D**). Their pro-fibrotic effect was consistent with the temporal pattern of expression of the mRNAs encoding their receptors (*PDGFRA, PDGFRB, TGFBR1, TGFBR2, TGFBR3, BMPR1B*) and intracellular signaling proteins (STATs, SMADs) (**Fig. S1**). The Clover$^+$ cells were distinct from hepatocytes and cholangiocytes; they co-expressed PDGFRβ, NCAM1 and COL1A1; and were located in various regions throughout the HO (**Fig. S2**).

The spatial distribution and morphology of the collagen fibers in HOs were examined using Second Harmonic Generation (**SHG**) microscopy [14,15], which has previously been used to quantitatively analyze liver fibrosis in human patients [16,17] and to monitor fibrosis in ARPKD HOs [12]. SHG images revealed that control HOs had sporadic networks of cross-linked collagen fibers surrounding the cells in some isolated regions, while the TGFβ1 or PDGF-treated organoids had more extensive networks of thick collagen fibers throughout the entire HO. A quantitative comparison indicated that TGFβ1 ($p < 0.05$) or PDGF ($p < 0.01$) exposure induced statistically significant increases in total collagen abundance and in the abundance of thick collagen fibers (i.e., > 3 um diameter) formed in HOs ($p<0.01$) (**Fig. 1E**). The SHG and immunostaining results indicate that PDGF or TGFβ1 increases the numbers of collagen synthesizing cells and the amount of thick collagen fibers formed in HOs.

*A high content screening system (**HCS**) for serially monitoring the effect of biochemical signals on liver fibrosis*. Culture conditions were modified to enable HOs to reproducibly grow to a standard size in microwells, which we refer to as '*microHOs*.' HCS was performed using a confocal fluorescence microplate imager with live cell fluidics and an automated program that we developed for analyzing multiple Z-stacked confocal images (**Fig. 2A-B**). TGFβ1 addition on day 13 induced a sustained increase in COL1A1$^+$ cells in microHOs that was blocked by co-

administration of TGFRβ1 tyrosine kinase inhibitors (10 uM SB431542 [18,19] or A83-01 [20]) (**Fig. 2C-D**). PDGFβ addition on day 13 also increased the number of COL1A1^{+} cells in microHOs, which was blocked by addition of a PDGFRβ tyrosine kinase inhibitor (10 uM Imatinib [21,22]) (**Fig. 3A**). The microHO system was also used to examine the effect of five cytokines (IL-4 [23], IL-6 [24], IL-13, IL-33 [25,26], TNFα [27]) and three growth factors (IGF1 [28], VEGF [29], CCL3 [30]) that had been directly or indirectly implicated in the pathogenesis of NASH or liver fibrosis. None of these agents induced fibrosis in microHOs (**Fig. S3**). Analysis of the temporal pattern of receptor expression in differentiating HO cultures using previously obtained transcriptomic data [12] revealed that the mRNAs encoding the IGF-1 (*IGF1R*), IL13 (*IL13RA1*), and VEGF (*VEGFR-1* (*FLT1*); *VEGFR-2 (KDR*)) receptors were expressed in day 9 hepatoblasts and in mature (day 21) organoids. In contrast, the mRNAs encoding the receptors for IL33 (*IL1RL1 or ST2*), IL4 (*IL4R*), or for the common gamma chain that is used for intra-cellular signaling by multiple cytokine receptors (*IL2RG*) were not expressed in day 9 hepatoblasts (**Fig. S4A**). Of note, the mRNAs encoding most of these receptors are abundantly expressed in mature HOs (**Fig. S4B**). Hence, the lack of a profibrotic effect of IGF-1 and VEGF is not due to the absence of receptor expression. However, the lack of a profibrotic effect for IL-4 and IL-13 could result from the absence of functional receptors at the time that the microHOs were exposed to those cytokines.

Since activation of the hedgehog signaling pathway has been shown to increase *COL1A1* mRNA expression in myofibroblasts [31,32] and to promote myofibroblast accumulation and liver fibrosis [33], we examined whether a hedgehog pathway activator would induce fibrosis in microHOs. Smoothened (**SMO**) is a seven transmembrane protein [34,35] that accumulates in the primary cilium, and transduces a Hedgehog pathway signal intracellularly. However, addition of a SMO agonist (SAG), which activates Hedgehog signaling [36], did not induce fibrosis in microHO cultures (Fig. S3).

We next examined whether addition of seven free fatty acids (at concentrations ranging from 0 to 400 uM), which included their saturated and corresponding cis-9 (or trans-9) monounsaturated forms, on day 13 to microHO cultures had a pro-fibrotic effect. Previously obtained transcriptomic data obtained from developing and mature HO cultures revealed that the mRNAs encoding proteins required for free fatty acid uptake (i.e., *SLC27A1, SCC27A5, FABP5, and Acyl-CoA Binding protein* (*ACBP*)) are expressed in day 9 HO cultures (**Fig. S5**). Even when the free fatty acids were added at concentrations below those previously reported to induce fibrosis in other types of HOs [37], the cells within microHOs abundantly accumulated fatty

acids from the medium and there was evidence of lipotoxicity (**Fig. S6**). Somewhat unexpectedly based upon the results presented in [37], free fatty acid addition did not have a pro-fibrotic effect in microHOs (**Fig. S7**). The disparate findings may result from their using organoid stiffness [37] (rather than an increase in collagen thick fibers) as the criteria for fibrosis. Our results, which are consistent with recent findings by others [38], indicate that free fatty acid addition causes steatosis and lipotoxicity, but does cause the fibrosis that develops during the advanced clinical stages of NASH. Altered differentiation conditions, adding other factors, or co-culture with other cell types may be required to enable HOs to model NASH-associated fibrosis.

Transcriptomic analysis. To molecularly characterize the pro-fibrotic effects of PDGFβ and TGFβ1, scRNA-Seq data was generated from day 9 control hepatoblast cultures (3832 cells), and from day 21 control (2587 cells), TGFβ1-treated (4091 cells) or PDGFβ-treated (2651 cells) microHOs. Fourteen cell clusters were identified from analysis of this data, and the hepatoblasts consisted of 4 closely related clusters (HB4-7) (**Fig. 4A, Table S1**). While the cells in control and PDGF-treated microHOs were quite similar, the cells in TGFβ1-treated microHOs were substantially different (**Fig. 4B**). The differentially expressed genes in each cluster cell were analyzed to identify the cell type for the clusters (**Tables S2-S3**). Control, PGDF- and TGFβ1-treated microHOs had comparable amounts of hepatocytes (Hep1-2), cholangiocytes (Cho1-2), endothelial cells and fetal erythrohepatoblasts. However, two mesenchymal clusters (Mes1-2) were far more abundant in control (56.5%) and PDGF-treated (53.4%) microHOs than in TGFβ1-treated (3.5%) microHOs, while the TGFβ1-treated microHOs had a much higher percentage of cells that resembled myofibroblasts (MyoF, 77%) than did control (3.4%) or PDGF-treated (4.5%) microHOs (**Fig. 4C**). The MyoF cluster uniquely expressed high levels of *Fibroblast Activation Protein Alpha (FAP)* and *Tissue inhibitor of metalloproteinases-1 (TIMP-1)* mRNAs, which is consistent with their being activated myofibroblasts (**Fig. 4D**). Consistent with their expression pattern in the clusters, FAP is absent in most tissues under basal conditions but is highly expressed on activated myofibroblasts [39,40]; and it is a well-established marker for activated fibroblasts [41]. FAP is a homodimeric type II integral membrane glycoprotein with a serine protease activity that mediates extracellular matrix degradation and tissue remodeling, and it promotes liver fibrosis by activating HSC and promoting macrophage infiltration after liver injury [42]. TIMP-1 is also produced by activated myofibroblasts; and because it inhibits ECM protein degradation by metalloproteinases (especially collagenases) [43-45], it plays a major role in determining the severity of liver fibrosis [46,47]. Circulating TIMP-1 levels are a marker for NASH [48] and for liver fibrosis of various etiologies [49,50]. The transcriptomic results indicate that TGFβ1

exposure converted mesenchymal cells into myofibroblast-like cells with a significantly increased level of expression of proteases, protease inhibitors and ECM proteins (**Table S4**).

Pharmacologic characterization of pro-fibrotic signaling pathways. PDGF and TGFβ1 are well established drivers of liver fibrosis [51]. TGFRB activation activates SMAD signaling pathways [52,53] and PDGFR cross-linking activates the STAT3 pathway [54 55], and both of these pathways have well-known roles in promoting hepatic fibrosis [55]. Since PDGFRβ and TGFβR1 inhibitors could block the PDGFβ and TGFβ1-induced increase in COL1A1$^+$ cells, respectively; the interaction between their intracellular signaling pathways was examined in microHOs. The TGFRβ inhibitor did not block the PDGFβ-induced increase, and the PDGFRβ inhibitor did not block the TGFβ1-induced increase in COL1A1$^+$ cells (**Fig. 3A-B**). Also, addition of the combination of PDGFβ and TGFβ1 did not significantly increase the number of COL1A1$^+$ cells in microHOs relative to that caused by either factor alone (Fig. 3B).

Although the anti-fibrotic effect of the receptor tyrosine kinase inhibitors was growth factor dependent, other signaling pathways that are jointly activated by the TGFβ1 and PDGF receptors could be essential for fibrosis. Both TGFRB [52,53,56] and PDGFR [57,58] activate the p38 Mitogen Activated Protein Kinase (MAPK) and PI3K–Akt–mTOR intracellular signaling pathways, which are also pro-fibrotic. Therefore, we examined whether co-administration of PI3K-Akt-mTOR (rapamycin) or MAPK pathway (SB202190) inhibitors with PDGF or TGFβ1 on day 13 could reduce fibrosis. Co-administration of 10 uM SB202190 – an ATP pocket binding and highly selective p38α and β kinase inhibitor [59] – inhibited both TGFβ1 and PDGF-induced fibrosis in microHOs (**Fig. 5A-C**). Thus, p38 MAPK pathway activity is essential for either PDGF- or TGFβ1-driven fibrosis. Rapamycin partially inhibited PDGF-induced fibrosis but did not inhibit TGFβ1-induced fibrosis (**Fig. 5D-F**) The lack of inhibition of TGFβ1-induced fibrosis by rapamycin indicated that the downstream part of the PI3K-Akt-mTOR pathway was not essential for TGFβ1-induced fibrosis, but it may be required for PDGF-induced fibrosis.

WNT/β-catenin signaling contributes to the pathogenesis of liver fibrosis and NASH [60,61], which led to the suggestion that it could be targeted by anti-fibrotic therapies [62]. Since glycogen synthase kinase 3β (GSK3β)-mediated phosphorylation of β-catenin targets it for ubiquitin-dependent proteasomal degradation, GSK3β inhibitors will stabilize β-catenin and promote the transcription of β-catenin target mRNAs [63,64]. Therefore, we examined the effect that co-

administration of Wnt/β-catenin pathway activators (R-spondin 1, Wnt3a) or a GSK3β enzyme inhibitor (10 uM CHIR99021) that has been shown to activate the Wnt/β-catenin pathway [65] had on fibrosis in microHOs. Co-administration of R-spondin-1 or Wnt3a had a very minimal effect on the extent of PDGF- or TGFβ1-driven fibrosis. The GSK3β inhibitor by itself did not increase $COL1A1^+$ cells in the organoids (Fig. S2). However, co-administration of the GSK3β inhibitor with either PDGF or TGFβ1 blocked fibrosis in microHOs (Fig. 3). Of importance, cell viability in microHOs was not reduced by TGFβ1 nor by adding the GSK3β or TGFRβ inhibitors**,** while the number of cells in the SB202190-treated microHOs was increased **(Fig. S9).** While the role of p38 MAPK in apoptosis has been debated, the SB202190-induced increase in the number of cells in microHOs is consistent with the ability of p38 to promote apoptosis in fibroblasts [66,67] and neutrophils [68]. Our results indicate that p38 MAPK or GSK3β kinase inhibitors can block liver fibrosis irrespective of whether it is driven by either PDGF or TGFβ1.

This microHO system could also be used to test the potential anti-fibrotic efficacy of candidate medications for liver fibrosis. For example, nintedanib and pirfenidone are the only two FDA-approved drugs for treatment of pulmonary fibrosis [69]. Both inhibit multiple tyrosine kinases and have been shown to reduce lung fibrosis in animal models [70-72] and in patients with interstitial lung fibrosis [73-75,76,77]. Although the mechanism for their anti-fibrotic effect is unknown, it has been suggested that they could also be used to treat liver fibrosis [55]. However, co-administration of 10 uM pirfenidone or 10 uM nintedanib did not inhibit the TGFβ1-induced fibrosis in microHOs. While pirfenidone did not inhibit PDGF-induced fibrosis, while nintedanib delayed the onset of PDGF-induced fibrosis in microHOs (**Fig. 5D-F**). Of note, the tested concentrations were >10-fold above the nintedanib concentration that inhibited PDGF-stimulated cellular proliferation (IC_{50} 64 nM) and PDGFR auto-phosphorylation (IC_{50} 22-39 nM) [78] and of the pirfenidone concentration (1 uM) that inhibited proliferation and TGFβ mRNA expression [79] in cultured human fibroblasts. The partial inhibitory effect of nintedanib of PDGF-induced fibrosis is consistent with its inhibition of the PDGF receptor tyrosine kinase activity (IC_{50} 60 nM) [80].

Discussion

We demonstrate that microHOs and the live cell imaging system developed here can be used to characterize the biochemical signals and intracellular signaling pathways that drive liver fibrosis and for assessing potential anti-fibrotic therapies. Of the twenty agents tested using microHOs –

which included cytokines, growth factors, fatty acids, a hedgehog agonist, and Wnt ligands – only PDGF and TGFβ1 had a strong pro-fibrotic effect. For several of the cytokines, growth factors and fatty acids tested, the absence of a pro-fibrotic effect in the organoid could be due to the absence of an immune system and/or of other cell types that could be required for a pro-fibrotic effect. However, a key finding emerging from this study is that the anti-fibrotic efficacy of PDGFR and TGFRβ tyrosine kinase inhibitors was dependent upon the factor driving the fibrosis, and this could explain why it has been so difficult to develop therapies for liver fibrosis. When fibrosis is driven by PDGFRβ-STAT3 pathway activation – as occurs in ARPKD liver fibrosis [12] or in murine models of lung and bone marrow fibrosis [81] – PDGFR inhibitors will exhibit anti-fibrotic efficacy; but they will be less effective when the fibrosis is driven by other mechanisms. There are organ-specific and species-specific differences in the mechanisms mediating tissue fibrosis [10] and different types of liver injury produces different patterns of liver fibrosis in humans [82]. Consistent with differences in the factors that drive different types of fibrosis, microHO data indicates that at least one (and possibly both) of the drugs that were FDA approved for treatment of lung fibrosis may not be effective when used for liver fibrosis. As another example, a combination treatment with PDGFR (imatinib) and TGFRβ (galunisertib [83]) inhibitors was more effective than blockade of either pathway alone in a murine radiation-induced lung fibrosis model [84]. To optimally treat liver fibrosis, therapies may have to be adjusted based upon the pathogenic driving factors, which may vary in different patients or in response to different inciting causes. There is already evidence that Diabetes patients can be subdivided into distinct sub-groups based upon clinical features and biomarker results [85], and efforts are underway to optimize treatment selection for the different types of diabetes patients [86]. Just as in other diseases, application of the principles of '*precision medicine'* (i.e., using genetic or genomic information to optimize treatment selection [87]) could enable therapies for liver fibrosis to be successfully developed.

Another key finding was that GSK3β and p38 MAPK inhibitors potently blocked the fibrosis induced by TGFβ1 or PDGF. The GSK3β inhibitor effect was unexpected since modulating Wnt/β-catenin signaling has had variable effects on liver fibrosis in mouse models [88,89]; and in a murine bile duct ligation model, GSK3β inhibitor administration produced an increase the extent of liver fibrosis [90]. As discussed in supplemental note 1, there are multiple nodes where the TGFβ, Wnt/β-catenin and the p38 MAPK pathways interact. These interactions could explain how a GSK3β inhibitor could block TGFβ-induced fibrosis; but the mechanism for the GSK3β

inhibitor effect on PDGF-induced fibrosis is less clear. Nevertheless, our results indicate that the p38 MAPK pathway, which is activated by both TGFβ1 and PDGF receptors, plays a key role in fibrosis. Although there was no prior data demonstrating that it had an effect on liver fibrosis, the ability of SB202190 to inhibit fibrosis in microHOs is consistent with prior studies showing that this agent inhibited the development of renal interstitial [91] and corneal [92] fibrosis in animal models, and the conversion of human corneal fibroblasts into myofibroblasts *in vitro* [93]. However, additional studies will have to be performed to characterize the mechanism(s) by which the Wnt/β-catenin and p38 MAPK pathways, along with the SMAD and STAT3 pathways that are also activated by TGFβ1 and PDGF receptors, jointly contribute to liver fibrosis. In summary, live cell imaging of human microHOs has identified GSK3β and p38 MAPK inhibitors as potential new therapies for liver fibrosis, and it is likely that other new therapies could subsequently be identified using this system.

Data availability. All raw and processed single cell RNA-seq data were deposited in the Gene Expression Omnibus (GEO) and are available under accession GSE228214.

Author Contributions. Y.G, S.R., A.H., P.K.J generated experimental data; Z.F., Y.G., P.K.J., A.E., S.C.H. and G.P. analyzed data; The paper was written by Y.G. and G.P with input from all authors.

References

1 Yoon, Y. J., Friedman, S. L. & Lee, Y. A. Antifibrotic Therapies: Where Are We Now? *Semin Liver Dis* **36**, 87-98 (2016). https://doi.org:10.1055/s-0036-1571295

2 Hernandez-Gea, V. & Friedman, S. L. Pathogenesis of liver fibrosis. *Annual review of pathology* **6**, 425-456 (2011). https://doi.org:10.1146/annurev-pathol-011110-130246

3 Pinzani, M. & Luong, T. V. Pathogenesis of biliary fibrosis. *Biochim Biophys Acta Mol Basis Dis* **1864**, 1279-1283 (2018). https://doi.org:10.1016/j.bbadis.2017.07.026

4 Pinzani, M. Pathophysiology of Liver Fibrosis. *Dig Dis* **33**, 492-497 (2015). https://doi.org:10.1159/000374096

5 Zhang, C. Y., Yuan, W. G., He, P., Lei, J. H. & Wang, C. X. Liver fibrosis and hepatic stellate cells: Etiology, pathological hallmarks and therapeutic targets. *World J Gastroenterol* **22**, 10512-10522 (2016). https://doi.org:10.3748/wjg.v22.i48.10512

6 Tsuchida, T. & Friedman, S. L. Mechanisms of hepatic stellate cell activation. *Nature reviews. Gastroenterology & hepatology* **14**, 397-411 (2017). https://doi.org:10.1038/nrgastro.2017.38

7 Yin, C., Evason, K. J., Asahina, K. & Stainier, D. Y. Hepatic stellate cells in liver development, regeneration, and cancer. *J Clin Invest* **123**, 1902-1910 (2013). https://doi.org:10.1172/JCI66369

8 Zhang, D. Y. *et al.* A hepatic stellate cell gene expression signature associated with outcomes in hepatitis C cirrhosis and hepatocellular carcinoma after curative resection. *Gut* **65**, 1754-1764 (2016). https://doi.org:10.1136/gutjnl-2015-309655
9 Mederacke, I. *et al.* Fate tracing reveals hepatic stellate cells as dominant contributors to liver fibrosis independent of its aetiology. *Nature communications* **4**, 2823 (2013). https://doi.org:10.1038/ncomms3823
10 Mehal, W. Z., Iredale, J. & Friedman, S. L. Scraping fibrosis: expressway to the core of fibrosis. *Nat Med* **17**, 552-553 (2011). https://doi.org:10.1038/nm0511-552
11 Guan, Y. *et al.* Human Hepatic Organoids for the Analysis of Human Genetic Diseases. *JCI Insight* **2**, pii: 94954 (2017). https://doi.org:10.1172/jci.insight.94954
12 Guan, Y. *et al.* A human multi-lineage hepatic organoid model for liver fibrosis. *Nature communications* **12**, 6138 (2021). https://doi.org:10.1038/s41467-021-26410-9
13 Schmid-Burgk, J. L., Honing, K., Ebert, T. S. & Hornung, V. CRISPaint allows modular base-specific gene tagging using a ligase-4-dependent mechanism. *Nature communications* **7**, 12338 (2016). https://doi.org:10.1038/ncomms12338
14 Campagnola, P. J. & Loew, L. M. Second-harmonic imaging microscopy for visualizing biomolecular arrays in cells, tissues and organisms. *Nat Biotechnol* **21**, 1356-1360 (2003). https://doi.org:10.1038/nbt894
15 Deniset-Besseau, A. *et al.* Measurement of the second-order hyperpolarizability of the collagen triple helix and determination of its physical origin. *J Phys Chem B* **113**, 13437-13445 (2009). https://doi.org:10.1021/jp9046837
16 Sun, W. *et al.* Nonlinear optical microscopy: use of second harmonic generation and two-photon microscopy for automated quantitative liver fibrosis studies. *J Biomed Opt* **13**, 064010 (2008). https://doi.org:10.1117/1.3041159
17 Gailhouste, L. *et al.* Fibrillar collagen scoring by second harmonic microscopy: a new tool in the assessment of liver fibrosis. *J Hepatol* **52**, 398-406 (2010). https://doi.org:10.1016/j.jhep.2009.12.009
18 Laping, N. J. *et al.* Inhibition of transforming growth factor (TGF)-beta1-induced extracellular matrix with a novel inhibitor of the TGF-beta type I receptor kinase activity: SB-431542. *Mol Pharmacol* **62**, 58-64 (2002). https://doi.org:10.1124/mol.62.1.58
19 Inman, G. J. *et al.* SB-431542 is a potent and specific inhibitor of transforming growth factor-beta superfamily type I activin receptor-like kinase (ALK) receptors ALK4, ALK5, and ALK7. *Mol Pharmacol* **62**, 65-74 (2002). https://doi.org:10.1124/mol.62.1.65
20 Tojo, M. *et al.* The ALK-5 inhibitor A-83-01 inhibits Smad signaling and epithelial-to-mesenchymal transition by transforming growth factor-beta. *Cancer Sci* **96**, 791-800 (2005). https://doi.org:10.1111/j.1349-7006.2005.00103.x
21 Puckett, R. L. *et al.* Maple syrup urine disease: further evidence that newborn screening may fail to identify variant forms. *Mol Genet Metab* **100**, 136-142 (2010). https://doi.org:10.1016/j.ymgme.2009.11.010
22 Breedveld, P. *et al.* The Effect of Bcrp1 (Abcg2) on the In vivo Pharmacokinetics and Brain Penetration of Imatinib Mesylate (Gleevec): Implications for the Use of Breast Cancer Resistance Protein and P-Glycoprotein Inhibitors to Enable the Brain Penetration of Imatinib in Patients. *Cancer Research* **65**, 2577-2582 (2005).
23 Weng, S. Y. *et al.* IL-4 Receptor Alpha Signaling through Macrophages Differentially Regulates Liver Fibrosis Progression and Reversal. *EBioMedicine* **29**, 92-103 (2018). https://doi.org:10.1016/j.ebiom.2018.01.028
24 Paquissi, F. C. Immunity and Fibrogenesis: The Role of Th17/IL-17 Axis in HBV and HCV-induced Chronic Hepatitis and Progression to Cirrhosis. *Front Immunol* **8**, 1195 (2017). https://doi.org:10.3389/fimmu.2017.01195

25 Marvie, P. *et al.* Interleukin-33 overexpression is associated with liver fibrosis in mice and humans. *J Cell Mol Med* **14**, 1726-1739 (2010). https://doi.org:10.1111/j.1582-4934.2009.00801.x
26 Tan, Z. *et al.* Interleukin-33 drives hepatic fibrosis through activation of hepatic stellate cells. *Cell Mol Immunol* **15**, 388-398 (2018). https://doi.org:10.1038/cmi.2016.63
27 Lu, S., Wang, Y. & Liu, J. Tumor necrosis factor-alpha signaling in nonalcoholic steatohepatitis and targeted therapies. *J Genet Genomics* **49**, 269-278 (2022). https://doi.org:10.1016/j.jgg.2021.09.009
28 Adamek, A. & Kasprzak, A. Insulin-Like Growth Factor (IGF) System in Liver Diseases. *International journal of molecular sciences* **19** (2018). https://doi.org:10.3390/ijms19051308
29 Mariotti, V., Fiorotto, R., Cadamuro, M., Fabris, L. & Strazzabosco, M. New insights on the role of vascular endothelial growth factor in biliary pathophysiology. *JHEP Rep* **3**, 100251 (2021). https://doi.org:10.1016/j.jhepr.2021.100251
30 Xu, L. *et al.* CC chemokine ligand 3 deficiency ameliorates diet-induced steatohepatitis by regulating liver macrophage recruitment and M1/M2 status in mice. *Metabolism: clinical and experimental* **125**, 154914 (2021). https://doi.org:10.1016/j.metabol.2021.154914
31 Hu, B. & Phan, S. H. Myofibroblasts. *Curr Opin Rheumatol* **25**, 71-77 (2013). https://doi.org:10.1097/BOR.0b013e32835b1352
32 Choi, S. S., Omenetti, A., Syn, W. K. & Diehl, A. M. The role of Hedgehog signaling in fibrogenic liver repair. *Int J Biochem Cell Biol* **43**, 238-244 (2011). https://doi.org:10.1016/j.biocel.2010.10.015
33 Syn, W. K. *et al.* Hedgehog-mediated epithelial-to-mesenchymal transition and fibrogenic repair in nonalcoholic fatty liver disease. *Gastroenterology* **137**, 1478-1488 e1478 (2009). https://doi.org:10.1053/j.gastro.2009.06.051
34 Chen, J. K., Taipale, J., Cooper, M. K. & Beachy, P. A. Inhibition of Hedgehog signaling by direct binding of cyclopamine to Smoothened. *Genes Dev* **16**, 2743-2748 (2002). https://doi.org:10.1101/gad.1025302
35 Taipale, J. *et al.* Effects of oncogenic mutations in Smoothened and Patched can be reversed by cyclopamine. *Nature* **406**, 1005-1009 (2000). https://doi.org:10.1038/35023008
36 Chen, J. K., Taipale, J., Young, K. E., Maiti, T. & Beachy, P. A. Small molecule modulation of Smoothened activity. *Proc Natl Acad Sci U S A* **99**, 14071-14076 (2002). https://doi.org:10.1073/pnas.182542899
37 Ouchi, R. *et al.* Modeling Steatohepatitis in Humans with Pluripotent Stem Cell-Derived Organoids. *Cell metabolism* **30**, 374-384 (2019). https://doi.org:10.1016/j.cmet.2019.05.007
38 Hendriks, D. *et al.* Engineered human hepatocyte organoids enable CRISPR-based target discovery and drug screening for steatosis. *Nat Biotechnol* (2023). https://doi.org:10.1038/s41587-023-01680-4
39 Levy, M. T., McCaughan, G. W., Marinos, G. & Gorrell, M. D. Intrahepatic expression of the hepatic stellate cell marker fibroblast activation protein correlates with the degree of fibrosis in hepatitis C virus infection. *Liver* **22**, 93-101 (2002). https://doi.org:10.1034/j.1600-0676.2002.01503.x
40 Gorrell, M. D. *et al.* Intrahepatic expression of collagen and fibroblast activation protein (FAP) in hepatitis C virus infection. *Adv Exp Med Biol* **524**, 235-243 (2003). https://doi.org:10.1007/0-306-47920-6_28
41 Lay, A. J., Zhang, H. E., McCaughan, G. W. & Gorrell, M. D. Fibroblast activation protein in liver fibrosis. *Front Biosci (Landmark Ed)* **24**, 1-17 (2019). https://doi.org:10.2741/4706

42 Yang, A. T. *et al.* Fibroblast Activation Protein Activates Macrophages and Promotes Parenchymal Liver Inflammation and Fibrosis. *Cell Mol Gastroenterol Hepatol* **15**, 841-867 (2022). https://doi.org:10.1016/j.jcmgh.2022.12.005
43 Benyon, R. C. & Arthur, M. J. Extracellular matrix degradation and the role of hepatic stellate cells. *Semin Liver Dis* **21**, 373-384 (2001). https://doi.org:10.1055/s-2001-17552
44 Iredale, J. P., Pellicoro, A. & Fallowfield, J. A. Liver Fibrosis: Understanding the Dynamics of Bidirectional Wound Repair to Inform the Design of Markers and Therapies. *Dig Dis* **35**, 310-313 (2017). https://doi.org:10.1159/000456581
45 Pellicoro, A., Ramachandran, P., Iredale, J. P. & Fallowfield, J. A. Liver fibrosis and repair: immune regulation of wound healing in a solid organ. *Nat Rev Immunol* **14**, 181-194 (2014). https://doi.org:10.1038/nri3623
46 Yoshiji, H. *et al.* Tissue inhibitor of metalloproteinases-1 promotes liver fibrosis development in a transgenic mouse model. *Hepatology* **32**, 1248-1254 (2000). https://doi.org:10.1053/jhep.2000.20521
47 Yoshiji, H. *et al.* Tissue inhibitor of metalloproteinases-1 attenuates spontaneous liver fibrosis resolution in the transgenic mouse. *Hepatology* **36**, 850-860 (2002). https://doi.org:10.1053/jhep.2002.35625
48 Wong, V. W., Adams, L. A., de Ledinghen, V., Wong, G. L. & Sookoian, S. Noninvasive biomarkers in NAFLD and NASH - current progress and future promise. *Nature reviews. Gastroenterology & hepatology* **15**, 461-478 (2018). https://doi.org:10.1038/s41575-018-0014-9
49 Czul, F. & Bhamidimarri, K. R. Noninvasive Markers to Assess Liver Fibrosis. *J Clin Gastroenterol* **50**, 445-457 (2016). https://doi.org:10.1097/MCG.0000000000000534
50 Agbim, U. & Asrani, S. K. Non-invasive assessment of liver fibrosis and prognosis: an update on serum and elastography markers. *Expert Rev Gastroenterol Hepatol* **13**, 361-374 (2019). https://doi.org:10.1080/17474124.2019.1579641
51 Frangogiannis, N. Transforming growth factor-beta in tissue fibrosis. *J Exp Med* **217**, e20190103 (2020). https://doi.org:10.1084/jem.20190103
52 Zhang, Y. E. Non-Smad Signaling Pathways of the TGF-beta Family. *Cold Spring Harbor perspectives in biology* **9** (2017). https://doi.org:10.1101/cshperspect.a022129
53 Budi, E. H., Duan, D. & Derynck, R. Transforming Growth Factor-beta Receptors and Smads: Regulatory Complexity and Functional Versatility. *Trends Cell Biol* **27**, 658-672 (2017). https://doi.org:10.1016/j.tcb.2017.04.005
54 Vignais, M. L. & Gilman, M. Distinct mechanisms of activation of Stat1 and Stat3 by platelet-derived growth factor receptor in a cell-free system. *Mol Cell Biol* **19**, 3727-3735 (1999). https://doi.org:10.1128/mcb.19.5.3727
55 Ying, H. Z. *et al.* PDGF signaling pathway in hepatic fibrosis pathogenesis and therapeutics (Review). *Mol Med Rep* **16**, 7879-7889 (2017). https://doi.org:10.3892/mmr.2017.7641
56 Budi, E. H., Schaub, J. R., Decaris, M., Turner, S. & Derynck, R. TGF-beta as a driver of fibrosis: physiological roles and therapeutic opportunities. *J Pathol* **254**, 358-373 (2021). https://doi.org:10.1002/path.5680
57 Razmara, M., Heldin, C. H. & Lennartsson, J. Platelet-derived growth factor-induced Akt phosphorylation requires mTOR/Rictor and phospholipase C-gamma1, whereas S6 phosphorylation depends on mTOR/Raptor and phospholipase D. *Cell Commun Signal* **11**, 3 (2013). https://doi.org:10.1186/1478-811X-11-3
58 Pan, S. *et al.* Platelet-derived PDGF promotes the invasion and metastasis of cholangiocarcinoma by upregulating MMP2/MMP9 expression and inducing EMT via the p38/MAPK signalling pathway. *Am J Transl Res* **12**, 3577-3595 (2020).

59 Frantz, B. *et al.* The activation state of p38 mitogen-activated protein kinase determines the efficiency of ATP competition for pyridinylimidazole inhibitor binding. *Biochemistry* **37**, 13846-13853 (1998). https://doi.org:10.1021/bi980832y
60 Annunziato, S., Sun, T. & Tchorz, J. S. The RSPO-LGR4/5-ZNRF3/RNF43 module in liver homeostasis, regeneration, and disease. *Hepatology* **76**, 888-899 (2022). https://doi.org:10.1002/hep.32328
61 Perugorria, M. J. *et al.* Wnt-beta-catenin signalling in liver development, health and disease. *Nature reviews. Gastroenterology & hepatology* **16**, 121-136 (2019). https://doi.org:10.1038/s41575-018-0075-9
62 Tian, L., Wang, Y. & Jang, Y. Y. Wnt signaling in biliary development, proliferation, and fibrosis. *Exp Biol Med (Maywood)* **247**, 360-367 (2022). https://doi.org:10.1177/15353702211061376
63 MacDonald, B. T., Tamai, K. & He, X. Wnt/beta-catenin signaling: components, mechanisms, and diseases. *Dev Cell* **17**, 9-26 (2009). https://doi.org:10.1016/j.devcel.2009.06.016
64 Nusse, R. & Clevers, H. Wnt/beta-Catenin Signaling, Disease, and Emerging Therapeutic Modalities. *Cell* **169**, 985-999 (2017). https://doi.org:10.1016/j.cell.2017.05.016
65 Sato, N., Meijer, L., Skaltsounis, L., Greengard, P. & Brivanlou, A. H. Maintenance of pluripotency in human and mouse embryonic stem cells through activation of Wnt signaling by a pharmacological GSK-3-specific inhibitor. *Nat Med* **10**, 55-63 (2004). https://doi.org:10.1038/nm979
66 Kummer, J. L., Rao, P. K. & Heidenreich, K. A. Apoptosis induced by withdrawal of trophic factors is mediated by p38 mitogen-activated protein kinase. *J Biol Chem* **272**, 20490-20494 (1997). https://doi.org:10.1074/jbc.272.33.20490
67 Xia, Z., Dickens, M., Raingeaud, J., Davis, R. J. & Greenberg, M. E. Opposing effects of ERK and JNK-p38 MAP kinases on apoptosis. *Science* **270**, 1326-1331 (1995). https://doi.org:10.1126/science.270.5240.1326
68 Alvarado-Kristensson, M. *et al.* p38-MAPK signals survival by phosphorylation of caspase-8 and caspase-3 in human neutrophils. *J Exp Med* **199**, 449-458 (2004). https://doi.org:10.1084/jem.20031771
69 Finnerty, J. P., Ponnuswamy, A., Dutta, P., Abdelaziz, A. & Kamil, H. Efficacy of antifibrotic drugs, nintedanib and pirfenidone, in treatment of progressive pulmonary fibrosis in both idiopathic pulmonary fibrosis (IPF) and non-IPF: a systematic review and meta-analysis. *BMC Pulm Med* **21**, 411 (2021). https://doi.org:10.1186/s12890-021-01783-1
70 Wollin, L. *et al.* Mode of action of nintedanib in the treatment of idiopathic pulmonary fibrosis. *Eur Respir J* **45**, 1434-1445 (2015). https://doi.org:10.1183/09031936.00174914
71 Iyer, S. N., Gurujeyalakshmi, G. & Giri, S. N. Effects of pirfenidone on transforming growth factor-beta gene expression at the transcriptional level in bleomycin hamster model of lung fibrosis. *J Pharmacol Exp Ther* **291**, 367-373 (1999).
72 Wang, Q. *et al.* Reduction of bleomycin induced lung fibrosis by transforming growth factor beta soluble receptor in hamsters. *Thorax* **54**, 805-812 (1999). https://doi.org:10.1136/thx.54.9.805
73 Richeldi, L. *et al.* Efficacy and safety of nintedanib in idiopathic pulmonary fibrosis. *N Engl J Med* **370**, 2071-2082 (2014). https://doi.org:10.1056/NEJMoa1402584
74 Flaherty, K. R. *et al.* Nintedanib in Progressive Fibrosing Interstitial Lung Diseases. *N Engl J Med* **381**, 1718-1727 (2019). https://doi.org:10.1056/NEJMoa1908681
75 Richeldi, L. *et al.* Efficacy of a tyrosine kinase inhibitor in idiopathic pulmonary fibrosis. *N Engl J Med* **365**, 1079-1087 (2011). https://doi.org:10.1056/NEJMoa1103690

76 Lancaster, L. H. *et al.* Pirfenidone safety and adverse event management in idiopathic pulmonary fibrosis. *Eur Respir Rev* **26** (2017). https://doi.org:10.1183/16000617.0057-2017
77 Costabel, U. *et al.* An Open-Label Study of the Long-Term Safety of Pirfenidone in Patients with Idiopathic Pulmonary Fibrosis (RECAP). *Respiration* **94**, 408-415 (2017). https://doi.org:10.1159/000479976
78 Wollin, L., Maillet, I., Quesniaux, V., Holweg, A. & Ryffel, B. Antifibrotic and anti-inflammatory activity of the tyrosine kinase inhibitor nintedanib in experimental models of lung fibrosis. *J Pharmacol Exp Ther* **349**, 209-220 (2014). https://doi.org:10.1124/jpet.113.208223
79 Lin, X., Yu, M., Wu, K., Yuan, H. & Zhong, H. Effects of pirfenidone on proliferation, migration, and collagen contraction of human Tenon's fibroblasts in vitro. *Invest Ophthalmol Vis Sci* **50**, 3763-3770 (2009). https://doi.org:10.1167/iovs.08-2815
80 Hilberg, F. *et al.* BIBF 1120: triple angiokinase inhibitor with sustained receptor blockade and good antitumor efficacy. *Cancer Res* **68**, 4774-4782 (2008). https://doi.org:10.1158/0008-5472.CAN-07-6307
81 Decker, M. *et al.* Leptin-receptor-expressing bone marrow stromal cells are myofibroblasts in primary myelofibrosis. *Nat Cell Biol* **19**, 677-688 (2017). https://doi.org:10.1038/ncb3530
82 Friedman, S. L. & Pinzani, M. Hepatic fibrosis 2022: Unmet needs and a blueprint for the future. *Hepatology* **75**, 473-488 (2022). https://doi.org:10.1002/hep.32285
83 Yingling, J. M. *et al.* Preclinical assessment of galunisertib (LY2157299 monohydrate), a first-in-class transforming growth factor-beta receptor type I inhibitor. *Oncotarget* **9**, 6659-6677 (2018). https://doi.org:10.18632/oncotarget.23795
84 Dadrich, M. *et al.* Combined inhibition of TGFbeta and PDGF signaling attenuates radiation-induced pulmonary fibrosis. *Oncoimmunology* **5**, e1123366 (2016). https://doi.org:10.1080/2162402X.2015.1123366
85 Ahlqvist, E. *et al.* Novel subgroups of adult-onset diabetes and their association with outcomes: a data-driven cluster analysis of six variables. *Lancet Diabetes Endocrinol* **6**, 361-369 (2018). https://doi.org:10.1016/S2213-8587(18)30051-2
86 Perreault, L., Skyler, J. S. & Rosenstock, J. Novel therapies with precision mechanisms for type 2 diabetes mellitus. *Nat Rev Endocrinol* **17**, 364-377 (2021). https://doi.org:10.1038/s41574-021-00489-y
87 Zeggini, E., Gloyn, A. L., Barton, A. C. & Wain, L. V. Translational genomics and precision medicine: Moving from the lab to the clinic. *Science* **365**, 1409-1413 (2019). https://doi.org:10.1126/science.aax4588
88 Zhuang, S. *et al.* Inhibition of GSK-3beta induces AP-1-mediated osteopontin expression to promote cholestatic liver fibrosis. *FASEB J* **32**, 4494-4503 (2018). https://doi.org:10.1096/fj.201701137R
89 Pradhan-Sundd, T. *et al.* Wnt/beta-Catenin Signaling Plays a Protective Role in the Mdr2 Knockout Murine Model of Cholestatic Liver Disease. *Hepatology* **71**, 1732-1749 (2020). https://doi.org:10.1002/hep.30927
90 Thompson, M. D. *et al.* beta-Catenin regulation of farnesoid X receptor signaling and bile acid metabolism during murine cholestasis. *Hepatology* **67**, 955-971 (2018). https://doi.org:10.1002/hep.29371
91 Prakash, J. *et al.* Intracellular delivery of the p38 mitogen-activated protein kinase inhibitor SB202190 [4-(4-fluorophenyl)-2-(4-hydroxyphenyl)-5-(4-pyridyl)1H-imidazole] in renal tubular cells: a novel strategy to treat renal fibrosis. *J Pharmacol Exp Ther* **319**, 8-19 (2006). https://doi.org:10.1124/jpet.106.106054

92 Nassar, K. *et al.* A p38 MAPK inhibitor improves outcome after glaucoma filtration surgery. *J Glaucoma* **24**, 165-178 (2015). https://doi.org:10.1097/IJG.0000000000000201

93 Guo, X., Sriram, S., Tran, J. A., Hutcheon, A. E. K. & Zieske, J. D. Inhibition of Human Corneal Myofibroblast Formation. *Invest Ophthalmol Vis Sci* **59**, 3511-3520 (2018). https://doi.org:10.1167/iovs.18-24239

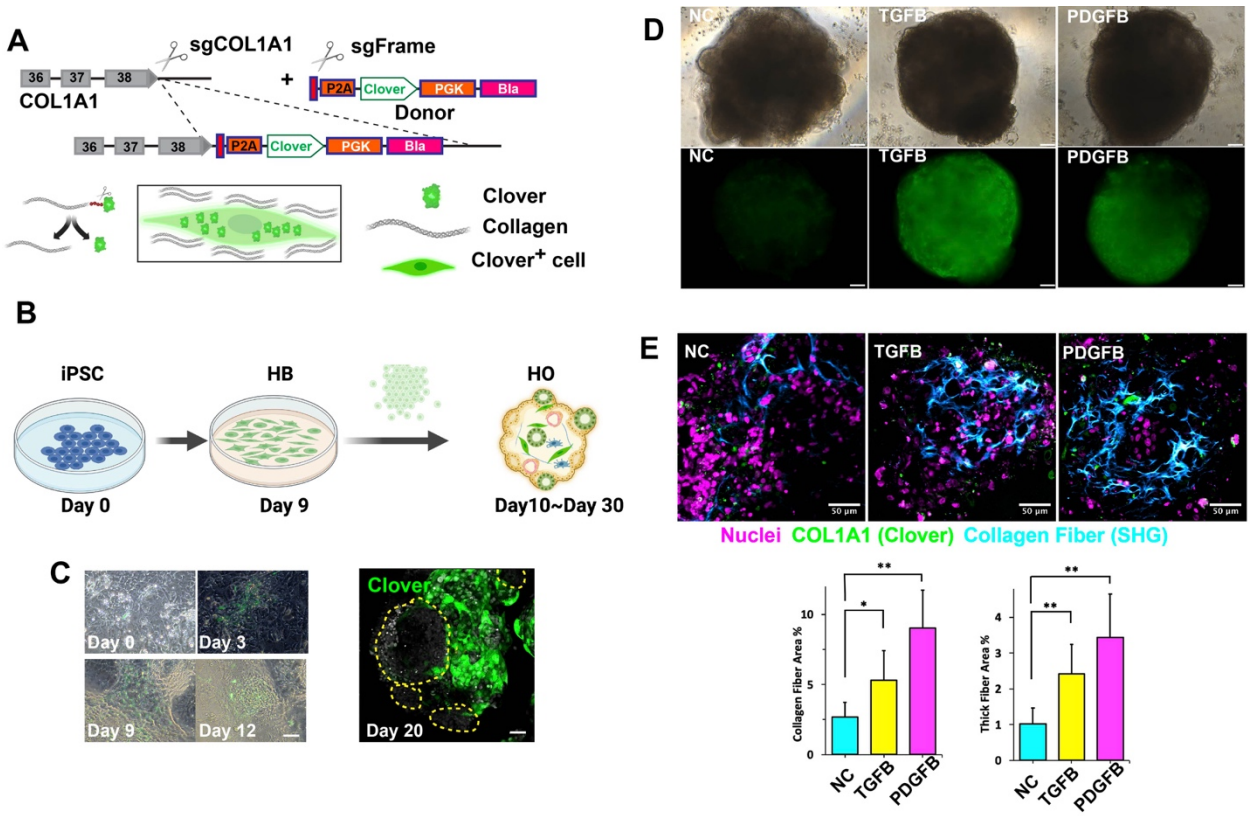

Figure 1. (A) *Top:* A diagram of the CRISPaint system used to insert P2A-Clover at the 3' end of *COL1A1* in an iPSC line. After blasticidin selection, cells were cloned to generate the COL1A1-P2A-Clover iPSC line. *Bottom*: The self-cleaving P2A peptide enables *COL1A1* expressing cells to be labelled with a fluorescent intracellular protein (Clover). (**B**) The collagen producing cells in a HO produced from COL1A1-P2A-Clover iPSCs are labelled with an intracellular fluorescent Clover protein. (**C**) *Left:* An overlay of bright field and fluorescent images of differentiating COL1A1-P2A Clover HO cultures reveals that the number of Clover$^+$ cells increase between days 3 and 12. Scale bar: 50 μm. *Right*: Confocal images show nuclei (DAPI stained) and Clover$^+$ fluorescent cells in day 20 COL1A1-P2A-Clover organoids. The yellow dashed circles indicate bile ducts. Clover$^+$ cells are not found within the bile ducts but are in other areas of the organoid. Scale bar: 50 μm. (**D**) Bright field (top) and immunofluorescence (bottom) images of day 21 *COL1A1*-P2A Clover HOs that were treated on day 13 with no addition (NC), 50 ng/ml TGFβ1 or 50 ng/ml PDGFβ. Both of these growth factors induced a marked increase in COL1A1$^+$ cells. Scale bars, 50 μm. (**E**) SHG analysis of the collagen fibers formed in human HOs. *Top:* Cross-sectional views of collagen fibers (cyan) and nuclei (magenta) in day 21 control organoids, or day 21 organoids that were treated on day 13 with 50 ng/ml TGFβ1 or 50 ng/ml PDGF. Control organoids (left) have isolated regions with relatively

thin collagen fibers (cyan). In contrast, the TGFβ1 or PDGF-treated organoids form a network of thick collagen fibers that extend throughout the entire organoid. Collagen producing cells (green) can also be seen in these images. Scale bars, 50 μm. *Bottom:* A quantitative comparison of collagen fiber area in SHG images was performed for control, TGFβ1- or PDGF-treated hepatic organoids ($n = 5$ organoids per category) on day 21. There is a statistically significant increase in total collagen abundance (% of collagen fiber area relative the total area of the imaged organoids) in the organoids after exposure to TGFβ1 (*, $p < 0.05$) or PDGF (**, $p < 0.01$, Welch's t-test). There was also a statistically significant increase in the abundance of thick collagen fibers (i.e., those fibers > 3 um diameter) in the TGFβ1 and PDGF-treated hepatic organoids.

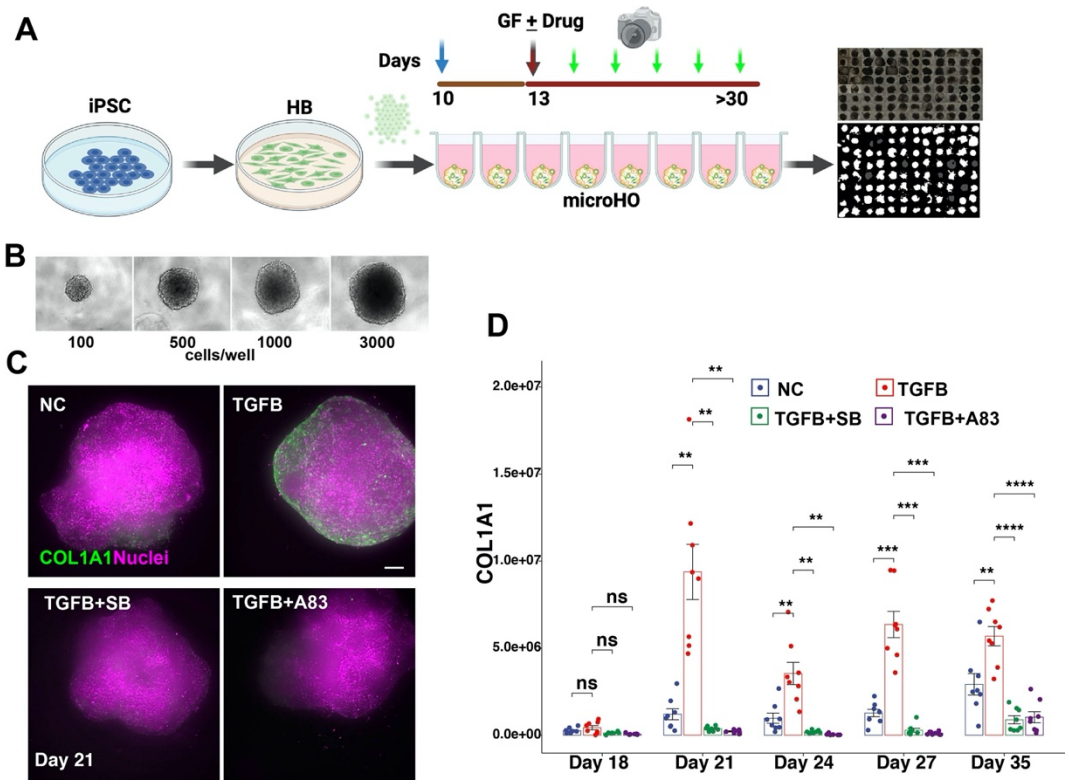

Figure 2. (**A**) A diagram of the HCS platform used for analysis of microHOs. COL1A1-P2A iPSCs are differentiated into hepatoblasts (HB), and 10,000 HBs are placed in each microwell on day 10. Growth factors (GF) and/or drugs are added on day 13, and the cultures are differentiated into hepatic organoids. Culture fluorescence is serially assessed to measure the number of COL1A1-producing cells in the microHO. Bright field (top) and fluorescence (bottom) images of a microwell plate with microHOs is shown on the right. (**B**) microHOs were produced by adding the indicated numbers of HBs to microwells. Bright field images on day 12 reveal that microHOs have a uniform shape and their size is dependent upon the number of input cells. (**C, D**) TGFβ1-induced fibrosis in microHOs is blocked by TGFRβ1 inhibitors. COL1A1-P2A Clover HOs were formed by adding 10,000 HBs to each microwell. Then, either nothing (NC), or 50 ng/ml TGFβ1 ± 10 uM TGFRβ1 inhibitors (SB431542 (SB) or A83-01 (A83)) was added to each microwell on day 13. (C) Maximum intensity projection (MIP) images of z stack sections obtained from the indicated type of microHOs on day 21. Scale bar 100 um. Clover expression is green, and nuclei stained with Hoechst 33342 are purple. (D) The amount of COL1A1^{+} cells within a microHO were serially measured on days 18 through 35. Each dot represents a measurement made on one microHO, 8 microHOs per treatment were assessed, and the box plots show the 25 to 75% range for all measurements per condition. The significance indicators are ns, not significant; *, p<0.05; **, p<0.01; ***, p<0.001 or ****, p<0.0001 for measurements in

TGFβ1 treated vs NC microHOs; and for microHOs that were treated with TGFβ1 and drug, the p-values are calculated relative to the TGFβ1 treated microHOs.

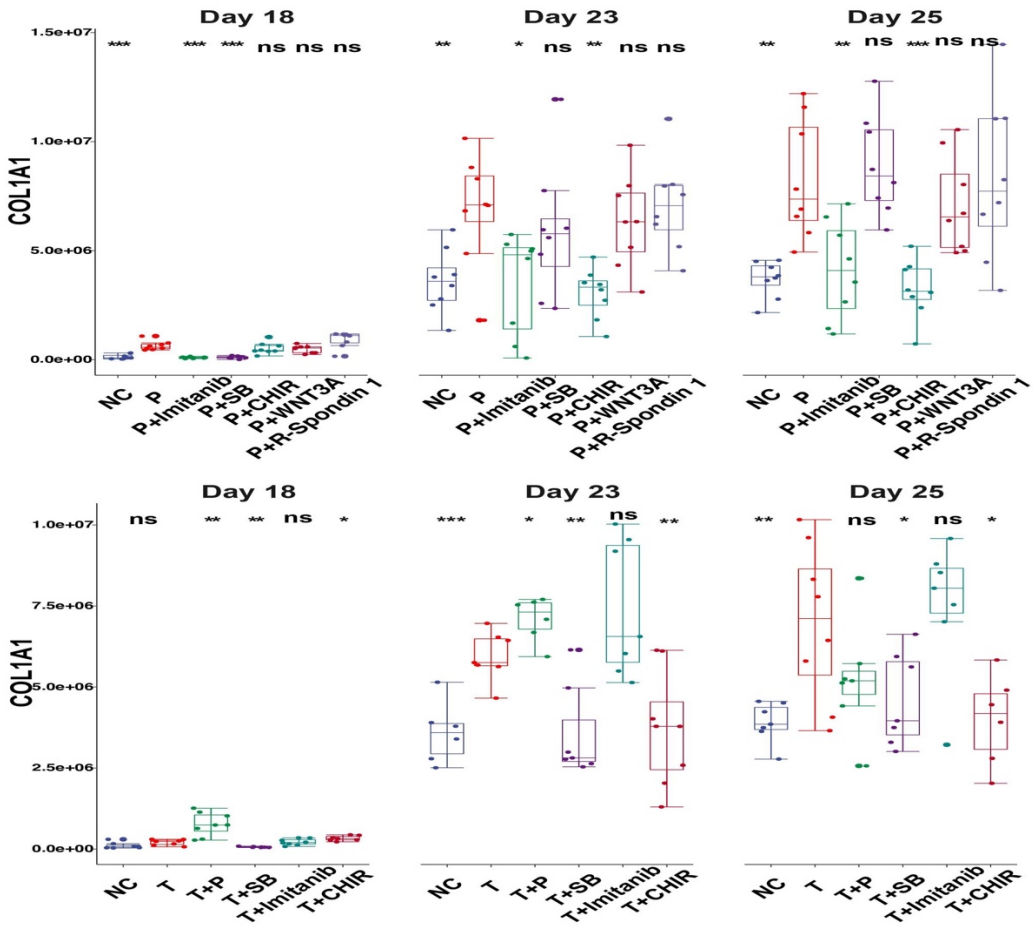

Figure 3. *Top:* The PDGFβ-induced increase in COL1A1^{+} cells is blocked by PDGFRβ and GSK3β inhibitors. *COL1A1*-P2A Clover HOs were formed by adding 10,000 cells from day 9 organoid cultures to each microwell. Then, either nothing (NC), 50 ng/ml PDGFβ (P) or 50 ng/ml PDGFβ with 10 μM imatinib, 10 uM SB431542 (SB), 10 uM CHIR99021 (CHIR), 100 ng/ml Wnt3a or 100 ng/ml R-spondin 1 was added to each microHO on day 13. *Bottom:* The TGFβ1 induced increase in COL1A1^{+} cells was blocked by TGFRβ and GSK3β inhibitors. Either nothing (NC), 50 ng/ml TGFβ1 (T), 50 ng/ml TGFβ1 with 50 ng/ml PDGF (T+P), or 50 ng/ml TGFβ1 and either 10 μM imatinib, 10 uM SB431542 (SB), or 10 uM CHIR99021 (CHIR) was added to each microHO on day 13. microHO fluorescence, which indicates the amount of COL1A1^{+} cells, was serially measured on days 18 through 25. Each dot represents a measurement made on a microHO, the thick line is the median for 8 microHOs that were assessed, and the box plot shows the 25 to 75% range for the measurements. In the panels: ns, not significant; *, $p<0.05$; or **, $p<0.01$, ***, $p<0.001$ for the measurement relative to the value in the NC; or when growth

factors or inhibitors were added, the p-values were calculated relative to that of the PDGFβ or TGFβ1 treated cultures.

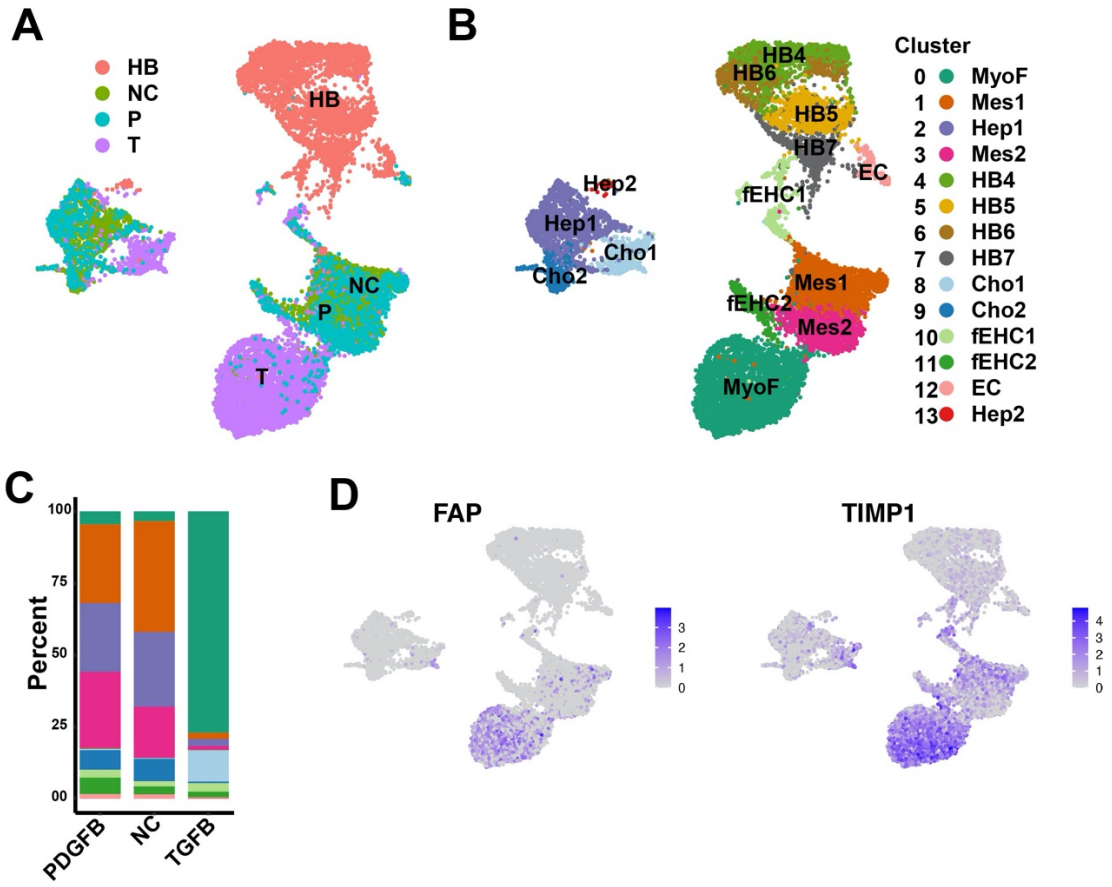

Figure 4. (**A**) combined sample u-MAP plot shows scRNA-seq data obtained from cells in day 9 hepatoblast (HB) cultures; or from day 21 control (NC), PDGFβ- (P) or TGFβ1 (T)-treated microHO cultures. The transcriptome of cells at the HB stage are distinct from those in the mature microHOs. *(***B**) The 14 different clusters identified by K-nearest neighbor analysis of the scRNA-Seq data shown in (A). Each cluster is indicated by a different color. The cell types were annotated based upon the genes shown in Table S2. Hepatoblasts consist of 4 similar clusters (HB4-7); there are two clusters of hepatocytes (Hep1-2) and cholangiocytes (Cho1-2); and there are endothelial cell (EC) and two fetal erythrohepatoblast (fEHC1-2) clusters. Two mesenchymal clusters (Mesen1-2) are more abundant in control and PDGF-treated microHOs, while the myofibroblasts (MyoF) are far more abundant in TGFβ1-treated microHOs than in control or PDGFβ1-treated microHOs. (**C**) The proportion of cells in clusters 0-13 in control, PDGF- or TGFβ1-treated microHOs are shown. (**D**) Feature plots show the level of expression of *FAP* and *TIMP1* mRNAs in the u-MAP plot shown in (B). The colors represent the $\log_2$-transformed level of expression of each mRNA. The myofibroblasts (cluster 0) have a markedly increased level of expression of both of these mRNAs.

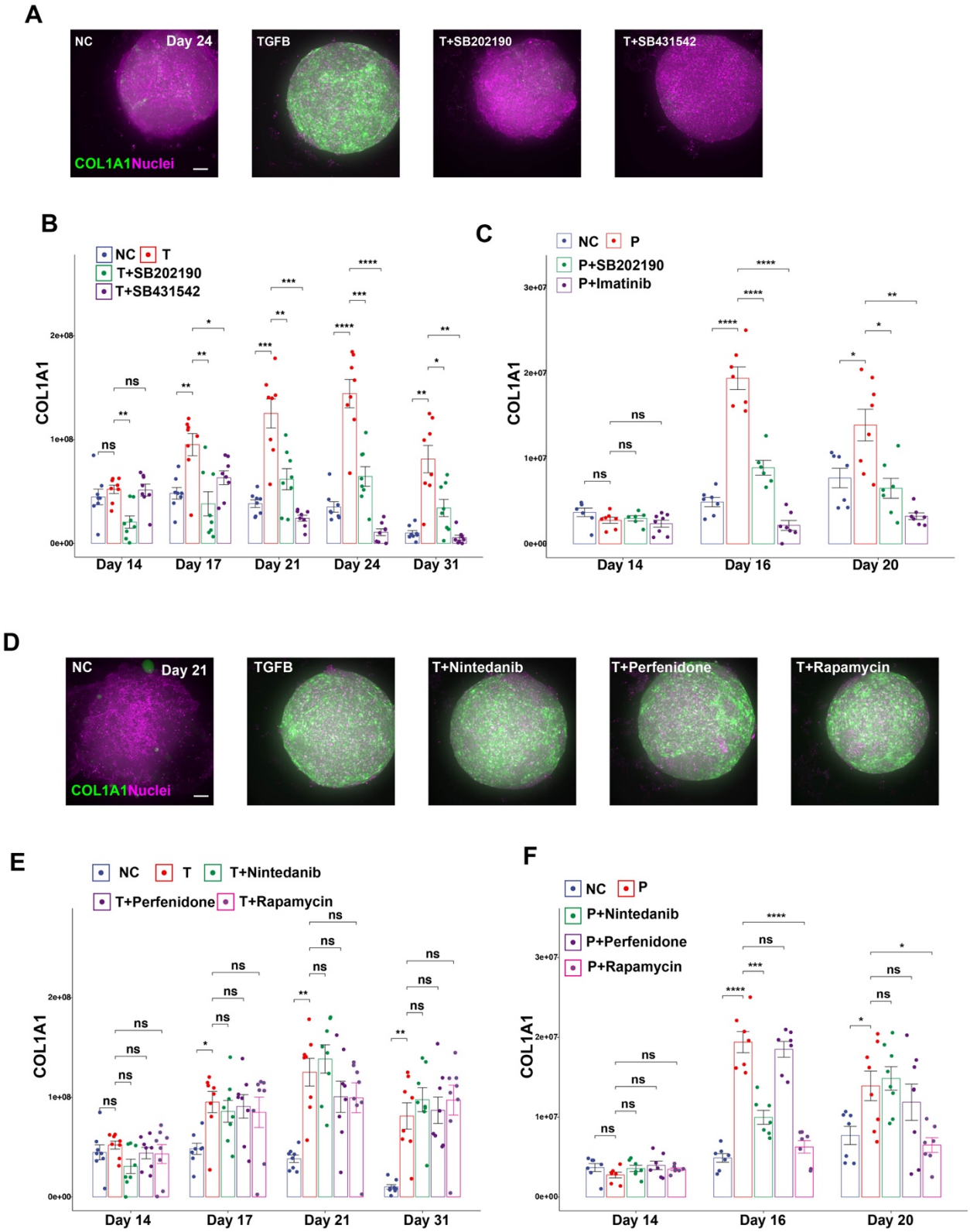
A
NC
Day 24
COL1A1Nuclei
TGFB
T+SB202190
T+SB431542
B
NC
T
T+SB202190
T+SB431542
COL1A1
Day 14
Day 17
Day 21
Day 24
Day 31
C
NC
P
P+SB202190
P+Imatinib
COL1A1
Day 14
Day 16
Day 20
D
NC
Day 21
COL1A1Nuclei
TGFB
T+Nintedanib
T+Perfenidone
T+Rapamycin
E
NC
T
T+Nintedanib
T+Perfenidone
T+Rapamycin
COL1A1
Day 14
Day 17
Day 21
Day 31
F
NC
P
P+Nintedanib
P+Perfenidone
P+Rapamycin
COL1A1
Day 14
Day 16
Day 20

Figure 5. TGFβ1- or PDGF-induced fibrosis in microHOs is inhibited by a p38 MAPK (SB202190) inhibitor (A-C); but only the PDGF-induced fibrosis is inhibited by pirfenidone or rapamycin (D-F). *COL1A1*-P2A Clover microHOs were formed by adding 10,000 HBs to each microwell. Then, either nothing (NC), 50 ng/ml TGFβ1 (T) or 50 ng/ml (PDGF) was added on day 13 to each microwell in the presence or absence of 10 uM of the following drugs: SB431542 (TGFRβ inhibitor), SB202190 (p38 α inhibitor), nintedanib, pirfenidone or rapamycin. (A, D) Maximum intensity projection (MIP) images of z stack sections obtained from microHOs treated with no addition (NC), or 50 ng/ml TGFβ ± 10 uM of the indicated drugs. Scale bar 100 um. Clover expression is green, and nuclei stained with Hoechst 33342 are purple. (B-C, E-F) The amount of $COL1A1^+$ cells within a microHO was serially measured on days 14 through 31. Each dot represents a measurement made on a microHO, the thick line is the median of 8 microHOs that were assessed, and the box plot shows the 25 to 75% range for all measurements per condition. When only growth factors were added, the p-values were relative to the NC, and the significance indicators are: ns, not significant; *, $p<0.05$; **, $p<0.01$; ***, $p<0.001$ or ****, $p<0.0001$. When growth factors and inhibitors were added, the p-values were calculated relative to the PDGFβ or TGFβ1 treated microHOs (without added drug).

Supplemental Information

Characterization of Pro-Fibrotic Signaling Pathways in Human Hepatic Organoids

Supplemental note 1: *Interactions between the TGFβ, Wnt/β-catenin and p38 MAPK pathways*. The TGFβ1 and Wnt/β-catenin pathways have several interaction points. (i) TGF-β significantly enhances hepatic WNT-5A expression *in vivo* and in myofibroblasts *in vitro* [1]. (ii) The interdomain regions of SMAD transcription factors have two residues that are phosphorylated by GSK3β in the nucleus, and their phosphorylation state regulates SMAD transcriptional activity and turnover [2]. Hence, the ability of the GSK3β inhibitor to block TGFβ1-induced fibrosis in microHOs could (at least in part) be mediated by altering the phosphorylation state of these two sites, which could alter SMAD transcription factor activity. (iii) During development, receptor tyrosine kinase and Wnt/β-catenin pathway signals were shown to be integrated by the level of SMAD phosphorylation [3].

The Wnt/β-catenin and p38 MAPK pathways also interact at several nodes. (i) Wnt ligands have been shown to activate p38 MAPK activity [4]. (ii) GSK3β phosphorylation by p38 MAPK regulates its kinase activity. MAPK kinases have a Thr–Gly–Tyr dual phosphorylation motif within their kinase activation loop, and both sites must be phosphorylated to fully activate the kinase. The MAP2K kinases MKK3 and MKK6 are the major upstream kinases for p38 activation [5]. However, phosphorylation on Ser^{389} on GSK3β is a major mechanism for downregulating its kinase activity and p38α was shown to inactivate GSK3β by this mechanism: p38-mediated phosphorylation of Ser^{389} on GSK3β was shown to cause β-catenin accumulation and activation of the Wnt signaling pathway [4,6]. By this mechanism, p38 MAPK inhibitors could reduce Wnt pathway activation, which could prevent the development of a fibrosis that was dependent upon Wnt signaling.

Materials and Methods

Chemicals. The growth factors, drugs, antibodies, and other staining reagents are shown in Tables S5-S6.

iPSCs and HO generation. The human iPSC line (C3) used in this study was prepared as previously described [7]. The biopsy sample used to generate this iPSC line was obtained according to a protocol (number 10368) approved by the Institutional Review Board at Stanford. The CRISPR-assisted insertion tagging system (CRISPaint) [8] plasmid (pCRISPR-HOT-Clover-

BlastR) was obtained from Addgene (Plasmid #138569; http://n2t.net/addgene:138569). A clover expression cassette (**P2A-Clover**) was inserted at the COOH terminus of the endogenous *COL1A1* gene of the iPSC line without a STOP code using a sgRNA (TTGGGATGGAGGGAGTTTAC). After Blasticidin selection, colonies obtained from single cells were picked and genotyped for the correct in-frame insertion using forward (actcccacgtggtaatgccc); and reverse (cttcagggtcagcttgccg) primers. iPSCs were differentiated into hepatic organoids (HOs) via culture in a series of media containing different growth factors using previously described methods [7].

Second Harmonic Generation (SHG) microscopy. SHG (collagen fibers) images from day 21 control, PDGF-treated and TGFβ1-treated HOs were collected on a multimodal nonlinear optical microscope setup, consisting of a modified inverted confocal microscope (Nikon, Ti2-E with C2 scanner and 60X water immersion objective, NA=1.27) and a picosecond-pulsed laser source (APE picoEmerald S, 2 ps pulse width, 80 MHz repetition rate, and 10 cm^{-1} bandwidth). As previously described[7], SHG data collection was made in the epi-direction with two narrow bandpass filters (Semrock FF01-400/12, Thorlabs MF390-18) and one shortpass filter (Thorlabs FESH0500). For the quantitative analyses, the area of the collagen fibers (identified by Otsu thresholding) was calculated for each SHG image and divided by the total sample area, forming the collagen area fraction (in %). To determine the diameter of the collagen fibers, the local thickness of the fibers was evaluated by applying the ImageJ Local Thickness routine (see the Analyze menu in Fiji) [9] to the SHG data. The volume fraction of thick collagen fibers (diameter ≥ 3 μm) was estimated by dividing the number of pixels represented by local thickness values ≥ 3 μm by the total number of pixels of the stack. To test whether the volume fractions obtained for control and TGFβ1- or PDGF-treated organoids were significantly different, the Welch's t-test was applied (* $p<0.05$ and ** $p<0.01$).

microHO generation. To produce microHOs, 50~60% confluent iPSC cultures were switched to an endoderm differentiation medium that consisted of DMEM/F12 + ITS (GIBCO) supplemented with 0.1 mM nonessential amino acids, 1 mM pyruvate and 2 mM L-alanyl-L-glutamine dipeptide (GlutaMAX). On days 1 to 2, 100 ng/ml Activin-A (Peprotech, Rocky Hill, NJ), 10 ng/ml BMP4 (Peprotech), 100 ng/ml bFGF (Peprotech), 3 mM CHIR99021 (Selleckchem, Houston, TX) and 10 uM LY294002 (Selleckchem) were added this medium. On day 3, 100 ng/ml Activin-A and 100 ng/ml bFGF were added the definitive endoderm differentiation medium. From days 4 to 9, 20 ng/ml FGF10 (Peprotech) and 20 ng/ml BMP4

were added to the hepatoblast medium, which consisted of which consisted of Advanced RPMI 1640 Medium (Gibco) that was supplemented with GlutaMAX and ITS. After day 9, the hepatoblasts were dissociated to single cells in Accutase (Invitrogen) medium with 10 uM Y-27632 (Santa Cruz Biotechnology, Dallas, Texas). Then, 1000 to 5000 cells/well were re-aggregated in low-cell-adhesion Nunclon™ Sphera™ 96 well Microplates (ThermoFisher) that contained serum-free HO growth and differentiation medium, which consisted of William's E medium supplemented with 0.1% Polyvinyl alcohol (Sigma-Aldrich), 0.1 mM nonessential amino acids, 1 mM pyruvate, 2 mM L-alanyl-L-glutamine dipeptide (GlutaMAX), 10 mM Y-27632, 100 ng/ml EGF, 10 ng/ml HGF, 10 μM Dexamethasone and 10 μM Hydrocortisone (Sigma, St. Louis MO). On day 13, 50 ng/ml of TGFβ1 (Peprotech, 100-21; or Sinobiological, 10804-HNAC) or 50 ng/ml of PDGFB (Miltenyibiotec, 130-108-163; or Peprotech, 100-14B) was added to each microwell.

microHO analysis. For COL1A1^{+} and Hoechst 33342 (Invitrogen, H3570) fluorescence measurements, 3D stacked images were captured from day 14 to day 31 cultures using a Molecular Devices ImageXpress Micro Confocal system. For confocal imaging20 to 40 planes crossing the whole organoid at 20 um intervals were captured using a 10X 0.45 Plan Apo 4mm WD objective with a 60-um pinhole. For each 10X confocal z-stack field (enough to cover one whole organoid), maximum intensity projections (MIPs) were generated from all of the acquired z-planes (the number planes ranged from 20 to 40 depending on the batch size). MIPs from each channel belonging to the same well were used for organoid segmentation and feature extraction by applying the machine learning based 'Trainable Weka Segmentation' [10] plugin from FIJI [11]. Each individual organoid edge was automatically segmented based on the nuclei signal (Hoechst 33342). Cell numbers were determined using the 'Find Maxima' function in defined area of an organoid after segmentation. COL1A1-P2A-Clover^{+} cells were segmented based on fluorescence. For training purposes, each analyzed element in every image (total 12 images) were used to train the classifiers by manual labelling all positive spots. Then, for experimental image analysis, the saved classifier was used to generate the probability map for each image. Segmented areas were then isolated, thresholded and binarized, and the Integrated Density was calculated from segmented area. An unpaired Student's t-test was used to test whether the measurements were significantly different between each comparison group. The macro script used for this analysis is available upon request.

Immunohistochemistry. Fresh organoids were harvested and fixed in 4% paraformaldehyde for 30 minutes. All organoids were either stained directly or embedded in low melting point agarose (IBI Scientific, Dubuque, Iowa). The primary antibodies used for staining are listed in Table S5. The organoids were stained with the primary antibody, and permeabilized by incubation with 1% Triton X-100 (Sigma-Aldrich, St. Louis, MO) and 10% chicken serum (Jackson ImmunoResearch, Bar Harbor, MA) overnight. Then, secondary antibody-staining was performed using an Alexa Fluor labeled chicken anti IgG (H+L), which was cross-adsorbed with a secondary antibody in 10% chicken serum (Invitrogen, Pleasanton, CA).

scRNA-Sequencing. Control, PDGFB- or TGFβ1-induced microHOs (n>30 per group) were harvested, and single cell suspensions were prepared by protease digestion as described [7]. The single cell suspensions were visually inspected under a microscope, cells were counted using a Scepter™ 2.0 Handheld Automated Cell Counter (EMD Millipore, Burlington, MA), and then resuspended in PBS with 0.01% BSA. scRNA-seq libraries were prepared by using the spit-pool based scRNA-seq method (Evercode™ WT Mini v2 from Parse biosciences) according to the manufacturer's instructions. In brief, ~5,000 cells from each group were split into 3 wells for the first round of sample barcoding, and the final pooled cells were divided into two equal libraries for sequencing. The expression matrix was generated using the 'Parse Biosciences analysis pipeline.' A total of 35,862 features that were generated from 13,160 cells were recovered from processing of the scRNA-seq data.

***scRNA-Seq data analysis*.** The scRNA-Seq data was imported into 'Seurat' [12] for the subsequent analysis steps. (i) Cells with unique gene counts <200 or where the percentage of mitochondrial mRNAs was >20% were removed. (ii) A total of 2000 variable genes were identified using the default settings. Unwanted sources of variation were removed by regression analysis, which was performed to mitigate the effect of signals caused by mRNAs with unique molecular identifiers and mitochondrial expression. (iii) Fifteen principal components were used to construct the shared nearest neighbor (SNN) graph, and the parameter regulating the resolution of the 'Find Clusters' program, was set to 0.6. This resulted in the identification of 14 unique clusters for all 13,160 cells. To identify the cell type of each cluster, differentially expressed genes for the pre-defined cell types were computed using the 'FindAllMarkers' function within the Seurat Package with the following parameters: only.pos = TRUE, min.pct = 0.25, logfc.threshold = 0.25. Seurat then identifies the differentially expressed genes using the non-parametric Wilcoxon rank sum test.

PathfindR (*github: egeulgen/pathfindR*) was used to perform the pathway enrichment analysis through identification of active subnetworks. Differentially expressed genes (which were analyzed to identify the cell type for each cluster) identified from the Seurat analysis were used as the input genes. In brief, a data frame consisting of the Gene Symbol, log-fold-change and adjusted-p values were used to perform the active subnetwork search. Pathway enrichment analyses was then performed using the genes identified within each of the identified active subnetworks using either the KEGG [13] or Reactome [14] database.

References

1 Beljaars, L., Daliri, S., Dijkhuizen, C., Poelstra, K. & Gosens, R. WNT-5A regulates TGF-beta-related activities in liver fibrosis. *Am J Physiol Gastrointest Liver Physiol* **312**, G219-G227, doi:10.1152/ajpgi.00160.2016 (2017).

2 Macias, M. J., Martin-Malpartida, P. & Massague, J. Structural determinants of Smad function in TGF-beta signaling. *Trends Biochem Sci* **40**, 296-308, doi:10.1016/j.tibs.2015.03.012 (2015).

3 Fuentealba, L. C. *et al.* Integrating patterning signals: Wnt/GSK3 regulates the duration of the BMP/Smad1 signal. *Cell* **131**, 980-993, doi:10.1016/j.cell.2007.09.027 (2007).

4 Bikkavilli, R. K., Feigin, M. E. & Malbon, C. C. p38 mitogen-activated protein kinase regulates canonical Wnt-beta-catenin signaling by inactivation of GSK3beta. *J Cell Sci* **121**, 3598-3607, doi:10.1242/jcs.032854 (2008).

5 Zarubin, T. & Han, J. Activation and signaling of the p38 MAP kinase pathway. *Cell Res* **15**, 11-18, doi:10.1038/sj.cr.7290257 (2005).

6 Thornton, T. M. *et al.* Phosphorylation by p38 MAPK as an alternative pathway for GSK3beta inactivation. *Science* **320**, 667-670, doi:10.1126/science.1156037 (2008).

7 Guan, Y. *et al.* Human Hepatic Organoids for the Analysis of Human Genetic Diseases. *JCI Insight* **2**, pii: 94954, doi:10.1172/jci.insight.94954 (2017).

8 Schmid-Burgk, J. L., Honing, K., Ebert, T. S. & Hornung, V. CRISPaint allows modular base-specific gene tagging using a ligase-4-dependent mechanism. *Nature communications* **7**, 12338, doi:10.1038/ncomms12338 (2016).

9 Hildebrand, T. & Ruegsegger, P. A new method for the model-independent assessment of thickness in three-dimensional images. *J. of Microscopy* **185**, 67-75 (1996).

10 Arganda-Carreras, I. *et al.* Trainable Weka Segmentation: a machine learning tool for microscopy pixel classification. *Bioinformatics* **33**, 2424-2426, doi:10.1093/bioinformatics/btx180 (2017).

11 Schindelin, J. *et al.* Fiji: an open-source platform for biological-image analysis. *Nat Methods* **9**, 676-682, doi:10.1038/nmeth.2019 (2012).

12 Butler, A., Hoffman, P., Smibert, P., Papalexi, E. & Satija, R. Integrating single-cell transcriptomic data across different conditions, technologies, and species. *Nat Biotechnol* **36**, 411-420, doi:10.1038/nbt.4096 (2018).

13 Kanehisa, M. & Goto, S. KEGG: kyoto encyclopedia of genes and genomes. *Nucleic Acids Res* **28**, 27-30 (2000).

14 Fabregat, A. *et al.* The Reactome pathway Knowledgebase. *Nucleic Acids Res* **44**, D481-487, doi:10.1093/nar/gkv1351 (2016).

15 Ramachandran, P. *et al.* Resolving the fibrotic niche of human liver cirrhosis at single-cell level. *Nature* **575**, 512-518, doi:10.1038/s41586-019-1631-3 (2019).
16 Guan, Y. *et al.* A human multi-lineage hepatic organoid model for liver fibrosis. *Nature communications* **12**, 6138, doi:10.1038/s41467-021-26410-9 (2021).

Cluster	Cell Type	% Control	% PDGF	% TGFβ1
0	MyoF	3.4	4.5	77.1
1	Mes1	38.7	27.4	2.2
2	Hep1	26	23.9	2.5
3	Mes2	17.8	26.5	1.3
4	HB	0	0	0
5	HB	0	0.07	0.02
6	HB	0	0.07	0.02
7	HB	0.08	0.15	0.04
8	Cho1	0.3	0.45	10.9
9	Cho2	7.8	6.8	0.5
10	fEHC1	1.8	2.7	3
11	fEHC2	2.7	5.7	2
12	EC	1.5	1.5	0.3
13	Hep2	0	0	0.1

Table S1. The cell types and the percentage of the total number of cells in the 14 cell clusters identified by analysis of scRNA-Seq data in control microHOs, and in PDGF- and TGFβ1-treated microHOs. The hepatoblasts (HB) in the day 9 cultures consisted of 4 closely related clusters (#4-7). The transcriptomes of the 10 other cell clusters in the day 21 microHOs were compared with the cells in control and cirrhotic human livers [15] using the Seurat label transfer function [12]. Based upon the level of concordance between the clusters and the sequences present in the previously defined cell types identified in human liver, the microHOs have cholangiocytes (Cho1-2, clusters 8-9), hepatocytes (Hep 1-2, clusters 2, 13), endothelial cells (EC, cluster 12) and fetal erythrohepatoblasts (fEHC1-2). Two mesenchymal clusters (Mesen1-2, clusters 1 and 3) were far more abundant in the control and PDGF-treated microHOs than in TGFβ1-treated microHOs, while the TGFβ1-treated microHOs had a much higher the percentage of myofibroblasts (MyoF, cluster 0) than control or PDGF-treated microHOs.

Cluster	Cell Type	Marker mRNAs
0	MyoF	*TIMP1, LTBP2, SERPINE2, FN1, SERPINE1,TIMP3, RUNX1, COL6A3, FAP, ALCAM*
1	Mesen1	*IL1RL1, DLK1,*
2	Hep1	*AFP, FGB, APOB, CKB, CFTR, CDH17, ALB, SERPINA1*
3	Mesen2	*SIPA1L2, CHRM2, RYR2, ADAMTS9*
4	HB	*FGFR2, CXCL14*
5	HB	*VIM, FLT1*
6	HB	*CCNB1, CCNB2*
7	HB	*MKI67, TOP2A*
9	Cho1	*SERPINA1, CYP1B1, HNF4A*
9	Cho2	*CDH6, ONECUT2, ONECUT1, SERPINA1, HNF4A, HHEX*
10	fEHC1	*C3, CPAMD8*
11	fEHC2	*EZR, ALPK1, CUL1, LRRC14, MAP3K8*
12	EC	*KDR, PECAM1, CD34, CDH5,VWF, FLT1*
13	Hep2	*APOB, HNF4A, AFP, FOXA2, APOA2, PDHB*

Table S2. The cell types for the 14 cell clusters were determined by analysis of the differentially expressed genes (shown in table S3) that were identified for each cluster. Selected mRNAs that are representative of the identified cell type for each cluster, which were identified using the 'FindAllMarkers' component of Seurat, are shown.

Table S3 is provided at the end of this file.

Table S4. Forty-two mRNAs whose expression was >2-fold greater in myofibroblasts (cluster 0) than mesenchymal cells (clusters 1 and 3). The gene symbol, p-value, adjusted p-value, and fold differential expression (log_2) for each differentially expressed gene are shown. Pct.1 and Pct.2 indicates the contribution of that feature to defining the indicated cluster based upon principal component analysis. The genes encoding proteases or protease inhibitors are in bold text (14% of total) and ECM proteins are in red text (12% of the total).

Gene	p val	pval adj	log2FC	Pct.1	Pct.2
NOX4	0	0	1.19	0.48	0.04
TIMP3	0	0	2.10	0.77	0.34
TIMP1	0	0	2.22	0.92	0.55
GLIS3	0	0	1.40	0.96	0.73
FN1	0	0	2.14	1.00	0.99
LTBP2	0	0	1.78	0.91	0.36
PMEPA1	0	0	1.27	0.92	0.44
PALLD	0	0	1.44	0.99	0.80
SERPINE2	0	0	1.21	0.98	0.79
BICD1	0	0	1.45	0.93	0.61
UBASH3B	0	0	1.82	0.80	0.24
RUNX1	0	0	1.33	0.95	0.62
COL6A3	0	0	1.54	0.96	0.68
SCG2	0	0	1.53	0.72	0.25
LAMA2	0	0	1.33	0.73	0.28
BMPR2	0	0	1.22	0.99	0.84
KANK4	4.62E-303	1.66E-298	1.24	0.56	0.12
UACA	6.11E-293	2.19E-288	1.14	0.89	0.59
SLC41A2	8.79E-277	3.15E-272	1.05	0.77	0.34
FAP	1.06E-275	3.79E-271	1.20	0.60	0.17
CALD1	1.82E-269	6.52E-265	1.11	0.96	0.80
COL4A2	3.80E-269	1.36E-264	1.04	0.96	0.74
TENM3	1.65E-259	5.90E-255	1.04	0.95	0.73
TPM1	7.71E-259	2.77E-254	1.02	0.91	0.62
DGKI	1.93E-254	6.91E-250	1.04	0.88	0.58
KLHL4	3.17E-251	1.14E-246	1.20	0.71	0.30
NTM	1.46E-250	5.25E-246	1.61	0.53	0.13
PDGFC	5.59E-245	2.00E-240	1.06	0.80	0.43

SEMA3C	3.92E-243	1.41E-238	1.14	0.75	0.35
HS3ST3A1	3.09E-240	1.11E-235	1.13	0.79	0.40
ADAMTS6	4.79E-229	1.72E-224	1.25	0.76	0.38
CILP	8.89E-219	3.19E-214	1.19	0.43	0.09
LTBP1	8.45E-216	3.03E-211	1.17	0.67	0.29
SMYD3	9.49E-201	3.40E-196	1.26	0.92	0.75
BICC1	1.73E-199	6.20E-195	1.01	0.74	0.39
GALNT13	5.38E-188	1.93E-183	1.01	0.67	0.30
SERPINE1	1.22E-186	4.38E-182	1.02	0.88	0.61
LNCAROD	1.56E-177	5.58E-173	1.30	0.45	0.13
LINC01060	6.85E-167	2.45E-162	1.01	0.38	0.09
LINC01705	1.29E-142	4.62E-138	1.10	0.26	0.03
NRG3	4.39E-142	1.58E-137	1.07	0.75	0.45
LINC00607	3.50E-132	1.26E-127	1.12	0.59	0.28

Table S5. Drugs and chemicals used in these studies.

Reagent	Company	Catalog #
palmic acid	SigmaAldrich	P5585
Oleic acid	SigmaAldrich	O1383
Stearic acid	SigmaAldrich	S4751
Myristic Acid	Caymanchem	13351
Myristoleic Acid	Caymanchem	9002461
Palmitoleic Acid	Caymanchem	10009871
Elaidic Acid	Caymanchem	90250
CDCA	SigmaAldrich	C9377
Activin A Protein	Sinobiological	10429-HNAH
Animal-Free Recombinant Human EGF	Peprotech	AF-100-15
EGF	Sinobiological	10605-HNAE
FGF4	Peprotech	100-31
HGF	Sinobiological	10463-HNAS
FGF10	Sinobiological	10573-HNAE
FGF2 Protein, Human, Recombinant	Sinobiological	10014-HNAE
FGF10	Peprotech	100-26
Human PDGF-BB IS	Miltenyibiotec	130-108-163
Human VEGF (165) IS	Miltenyibiotec	130-109-383
Recombinant Human PDGF-BB (carrier-free)	Biolegend	577302
Recombinant Human PDGF-BB	Peprotech	100-14B
Recombinant Human PDGF-BB Protein, CF	rndsystems	220-BB-010In Stock
TGF beta 1 Protein, Human, Rhesus, Cynomolgus, Canine, Recombinant	Sinobiological	10804-HNAC
Recombinant Human BMP-4	Peprotech	120-05
Recombinant Human BMP-4 (carrier-free)	Biolegend	795606
Recombinant Human/Mouse/Rat Activin A	R&D	338-AC-010
Recombinant Human FGF-Basic (146 a.a.)	Peprotech	AF-100-18C
Wnt3a	Peprotech	315-20
OSM	Peprotech	300-10
IL3 Protein, Human, Recombinant (His Tag)	Sinobiological	11858-H08H
IL6	R&D	7270-IL-010/CF
IL-13 Protein, Human, Recombinant	Sinobiological	10369-HNAC
IL-33 Protein, Human, Recombinant	Sinobiological	10368-HNAE
IGF1	R&D	291-G1-200
R-Spondin 1 Protein	R&D	4645-RS
JAG-1 protein	StemRD	Cat#: JAG-1-pep-100
SB202190 (FHPI)	Selleckchem	S1077
SB431542	Selleck	S1067
Sirolimus (Rapamycin)	Medkoo	100766
Imatinib mesylate	Medkoo	100470
DAPT (GSI-IX)	Selleckchem	S2215
LDN-193189	Selleckchem	S2618
SAG	Selleckchem	S7779
IWR1-en	Selleckchem	S7086
A-83-01	Santa Cruz Biotechnology	sc-203791
PI-103	Tocris	2930
PD0325901	Santa Cruz Biotechnology	sc-205427
CHIR99021	Tocris	4423
Wnt-C59	Tocris	5148
BIO	Selleckchem	S7198
Thiazovivin	Medchemexpress	HY-13257
Nintedanib	Tocris	7049
Pirfenidone	Tocris	1093
polyvinyl alcohol	SigmaAldrich	P8136
Matrigel	BD	354234

Table S6. Antibodies and staining reagents used in these studies.

Antibody	Company	Catalog #	Dilution
CK8	abcam	(ab53280)	1/100 - 1/250
CK8	DSHB	(TROMA-I)	200
COL1	ABCAM	(ab34710)	1:100
GFP Tag Polyclonal Antibody	thermofisher	A-11122	200-2000
GFP Antibody (B-2)	scbt	sc-9996	50
Human Albumin Antibody	Bethyl	A80-129A	1:200 – 1:2,000
PDGFRB	eBioscienc	14-1402-82	100
PDGFRB	ABCAM	(ab32570)	100
PDGFRB	R&D	AF385-SP	100
PDGFRB	Signaling Techn	3169T	100
LipidSpot™ Lipid Droplet Stains	biotium	#70069-T	
MitoSox Red	Invitrogen	M36008	

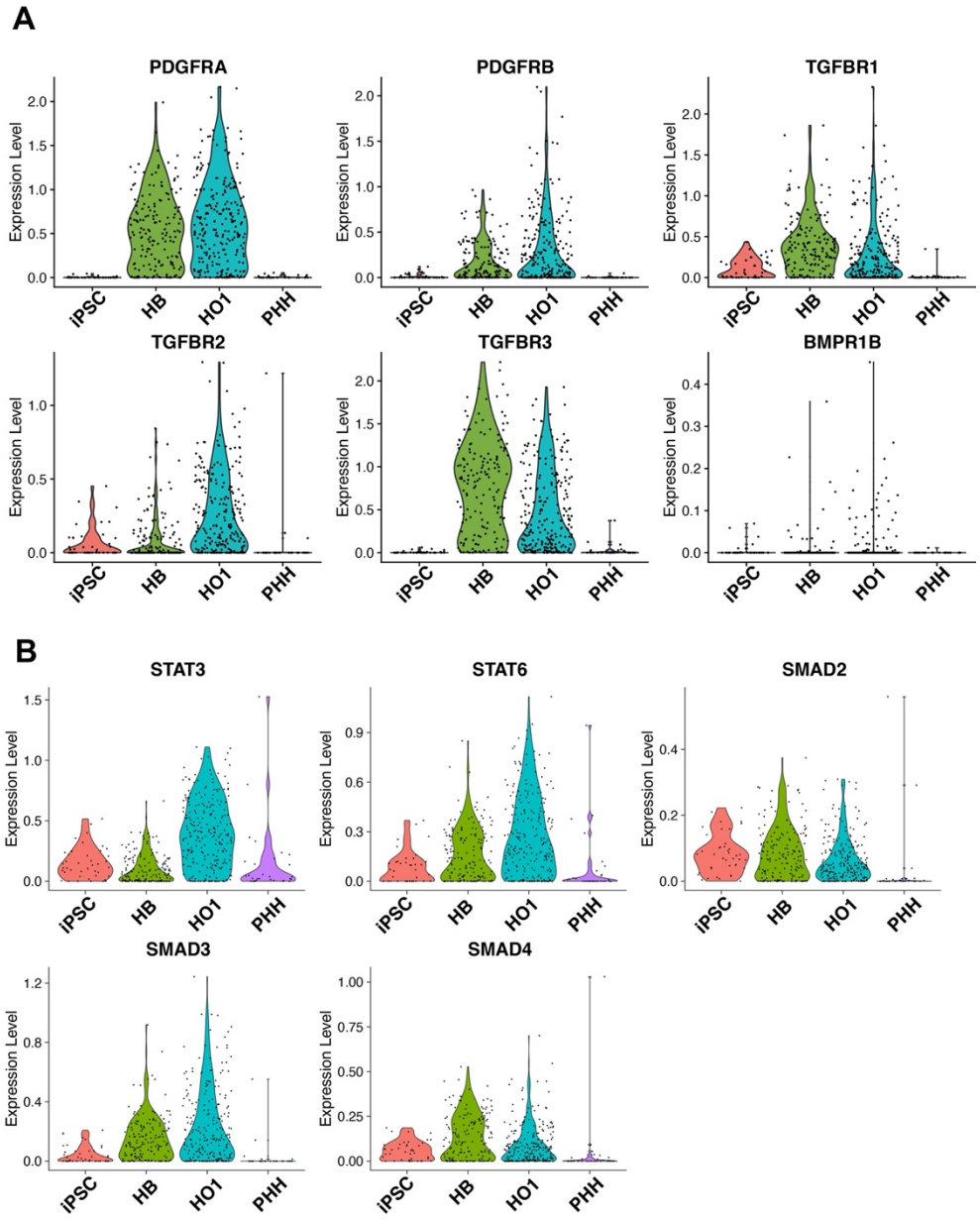

Figure S1. (**A, B**) Violin plots showing the level of expression of mRNAs encoding the receptors for PDGF (*PDGFRA, PDGFRB*) and TGFβ1 (*TGFBR1, TGFBR2, TGFBR3, BMPR1B*); and of *STAT3*, *STAT6*, and *SMAD2-4* mRNAs in developing and mature HO cultures. scRNA-Seq data was generated from iPSC (day 0), day 9 hepatoblast (HB) and day 21 mature organoid cultures. For comparison purposes, scRNA-Seq data obtained from primary human hepatocytes (PHH) is also shown.

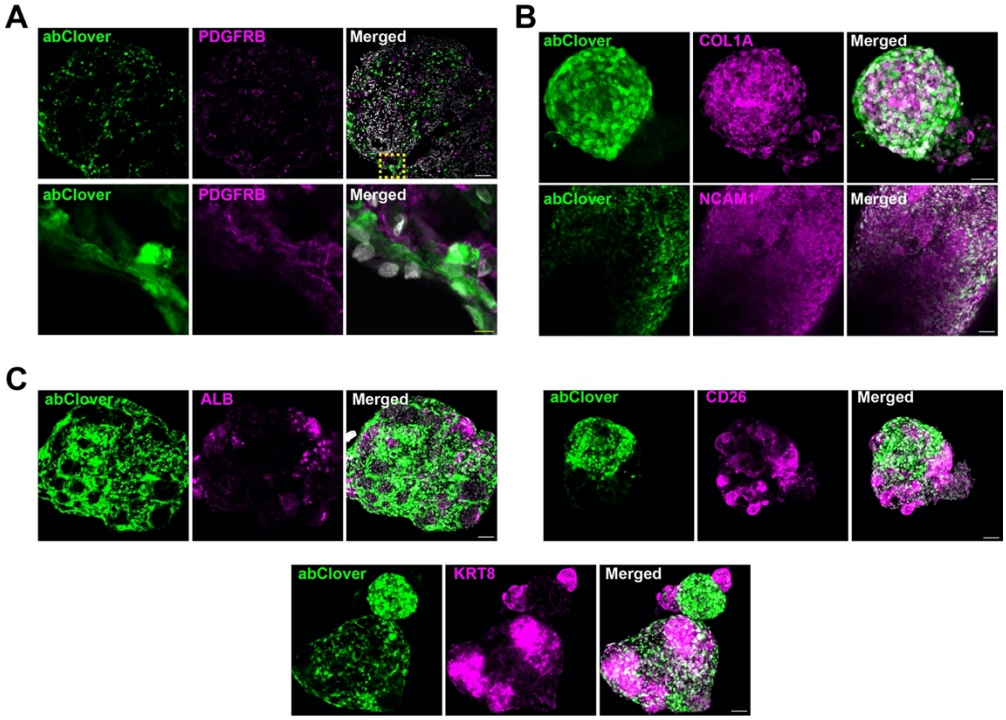

Figure S2. Immunofluorescent images of day 20 *COL1A1*-P2A Clover HOs that were stained with antibodies to Clover (GFP) and PDGFRB (**A**); or to Clover, COL1A and NCAM1 (**B**); or Clover ALB, CD26 and KRT8 (**C**). As seen in the merged images, the Clover$^+$ cells are distinct from the ALB$^+$, KRT8$^+$ and CD26$^+$ hepatocytes and cholangiocytes; while PDGFRB, COL1A and NCAM1 are co-expressed in the Clover$^+$ cells. Scale bars, 50 μm.

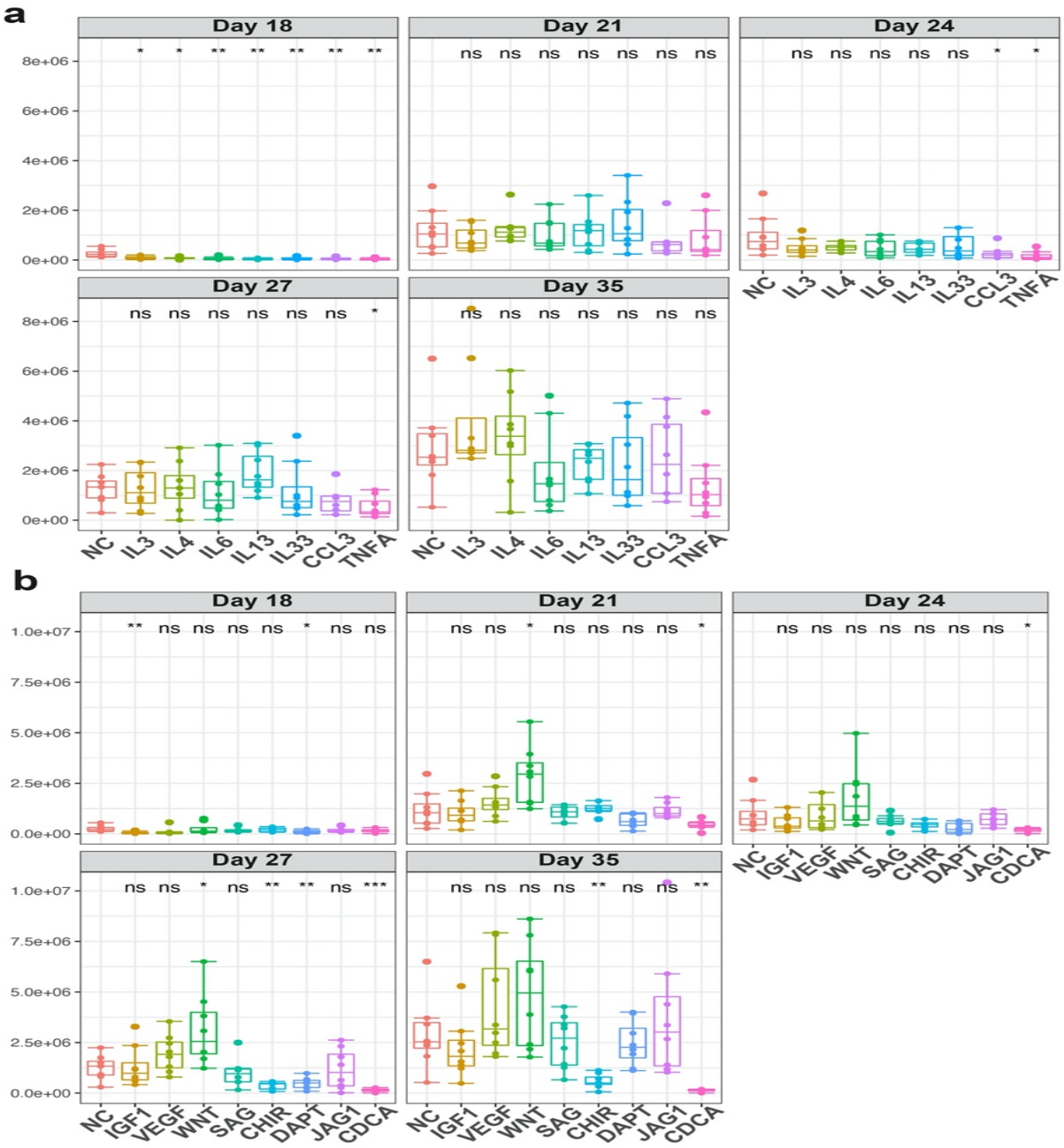

Figure S3. *COL1A1*-P2A Clover HOs were incubated with (**A**) 100 ng/ml IL-3, 100 ng/ml IL-4, 100 ng/ml IL-6, 100 ng/ml IL13, 100 ng/ml IL-33, 100 ng/ml CCL3, 50 ng/ml TNFa; or (**B**) 100 ng/ml IGF1, 50 ng/ml VEGF, 100 ng/ml Wnt3a, 10 μM SAG (Smoothened agonist), 3 μM CHIR99021, 10 μM DAPT (Gamma-Secretase Inhibitor), 100 ng/ml JAG1, 10 μM chenodeoxycholic acid (CDCA), or no addition (NC). Culture fluorescence, which indicates the

amount of COL1A1^{+} cells in the HOs, was serially measured on days 18 through 35. Each dot represents a measurement made on one HO, the thick line is the median of 8 organoids analyzed per condition, and the box plot shows the 25 to 75% range for all measurements per condition. With the possible exception of Wnt3a, none of these added agent caused a significant and or a sustained increase in COL1A1^{+} cells in any of the organoid cultures. CDCA induced a decrease in COL1A1^{+} cells.

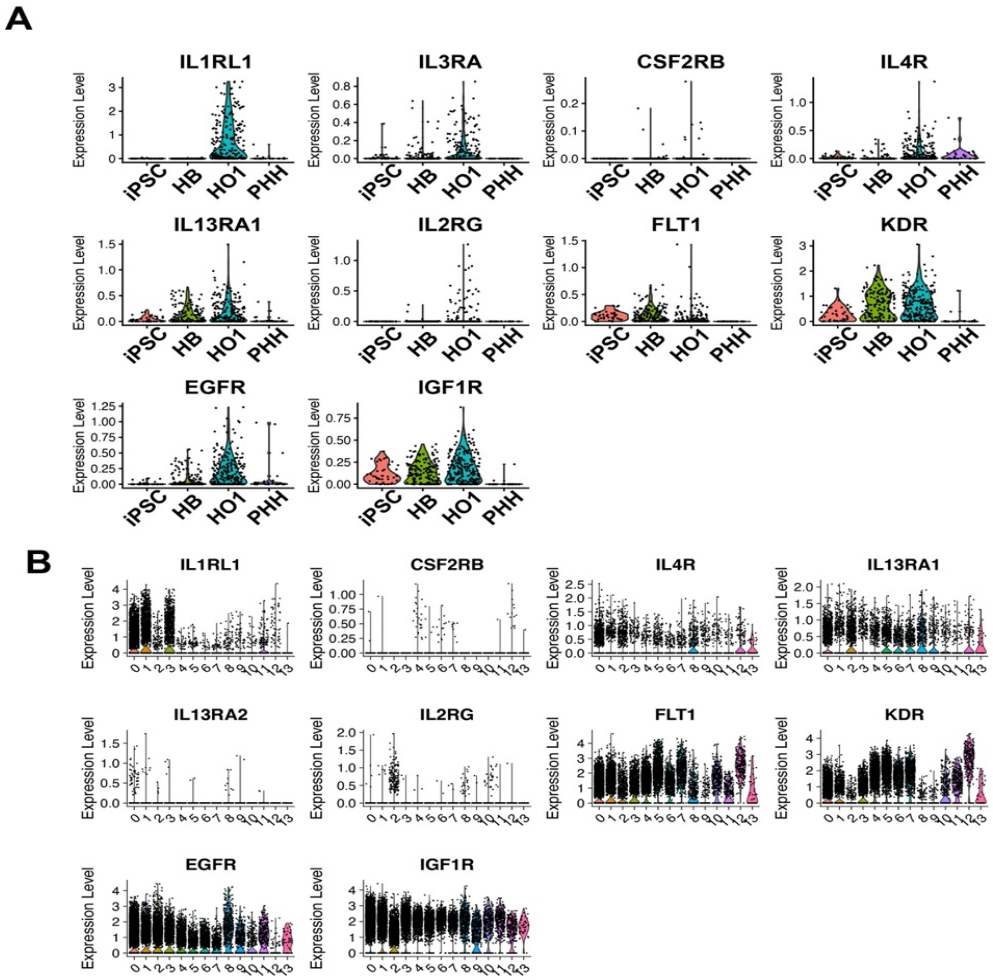

Figure S4. (**A**) Violin plots showing the level of expression of mRNAs for the following receptors during HO development: *IL1RL1, IL4R, IL13RA1, IL2RG, FLT1, KDR,* and *IGF1R*. scRNA-Seq data was generated from iPSC (day 0), day 9 hepatoblast (HB) and day 21 mature organoid (HO1) cultures. For comparison purposes, scRNA-Seq obtained from primary human hepatocytes (PHH) is also shown. The scRNA-Seq data was obtained from [16]. (**B**) Violin plots showing the level of mRNA expression for the receptors shown in (A) in 14 cell clusters identified in microHOs.

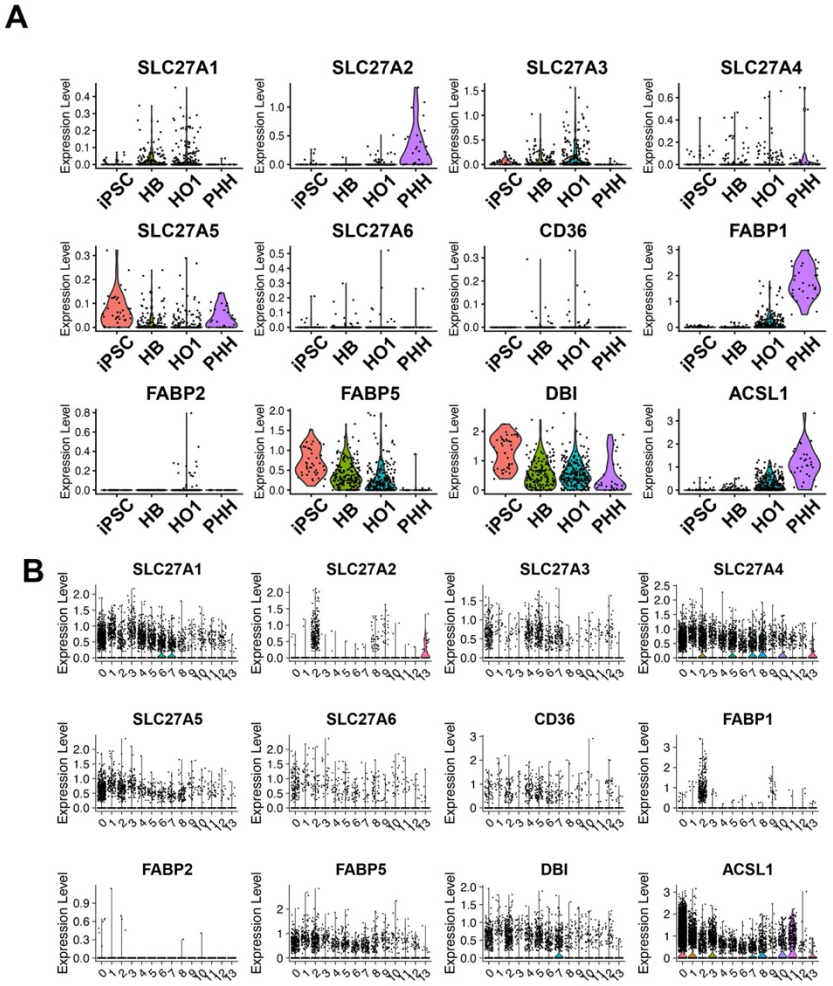

Figure S5. (**A**) **A**) Violin plots showing the level of expression of mRNAs for the following fatty acid transport proteins during HO development: *SLC27A1-6, CD36, FABP1-2, FABP5, DBI* and *ACSLI.* scRNA-Seq data was generated from iPSC (day 0), day 9 hepatoblast (HB) and day 21 mature organoid cultures. For comparison purposes, scRNA-Seq obtained from primary human hepatocytes (PHH) is also shown. (**B**) Violin plots showing the level of mRNA expression for the for the fatty acid transport proteins shown in (A) in 14 cell clusters identified in mature day 21 hepatic organoids.

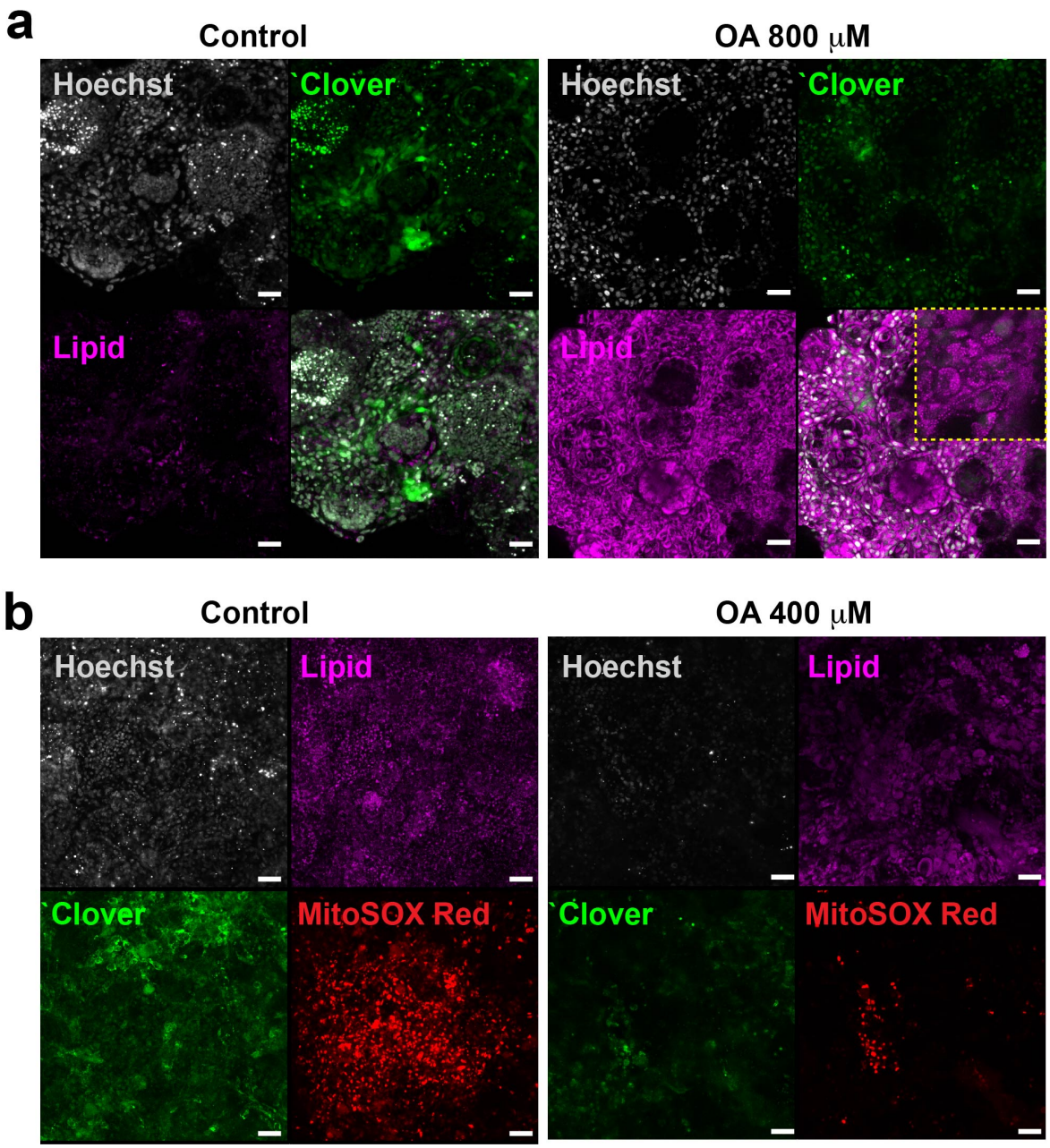

Figure S6. Oleic acid (OA) induces toxicity in HOs. Either 800 (**A**) or 400 (**B**) uM OA was added to HO cultures on day 13, and the HOs were analyzed by the HCS system on day 24. Although there was a marked increase in intracellular fatty acids within the HOs that were incubated with OA (LipidSpot), OA addition did not increase in COL1A1 expression (Clover). Moreover, there was a marked decrease in cell viability within the HOs that were incubated with OA, as shown by the MitoSox Red analysis.

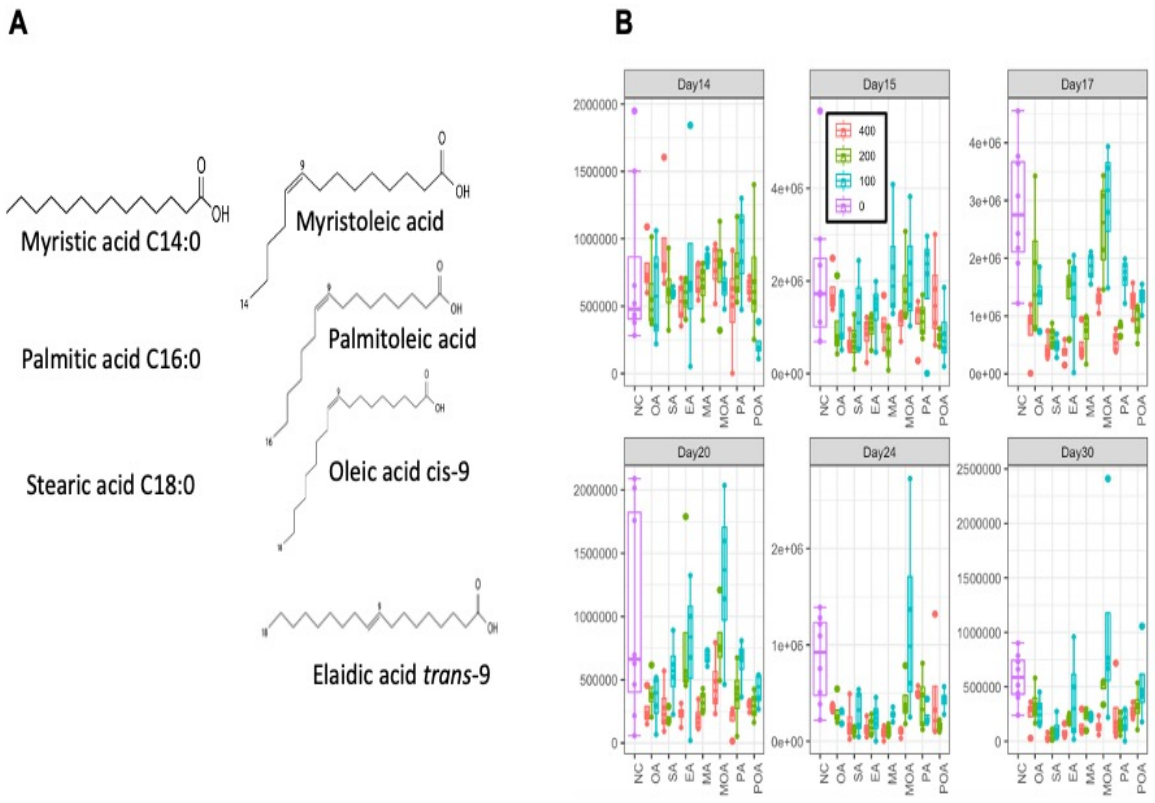

Figure S7. Free fatty acids do not increase collagen expression in HOs. (**A**) The structures of the free fatty acids whose effect on collagen expression in HOs was analyzed. Unsaturated FFAs (myristic (MA), palmitic (PA) and stearic (SA)) and their corresponding FFA with cis-9 (Myristoleic (MOA), palmitoleic (POA), and oleic (OA)) or trans-9 (elaidic (EA)) double bonds were analyzed. (**B**) *COL1A1*-P2A Clover HOs were incubated with 0, 100, 200 or 400 uM of the indicated free fatty acid on day 13. The fluorescence in these cultures, which indicates the amount of COL1A1^{+} cells in the HOs, was serially measured on days 14 through 30. Each dot represents a measurement made on one HO, the thick line is the median of 8 organoids analyzed per condition, and the box plot shows the 25 to 75% range for all measurements per condition. The free fatty acids did not induce a significant increase in COL1A1^{+} in any of the cultures.

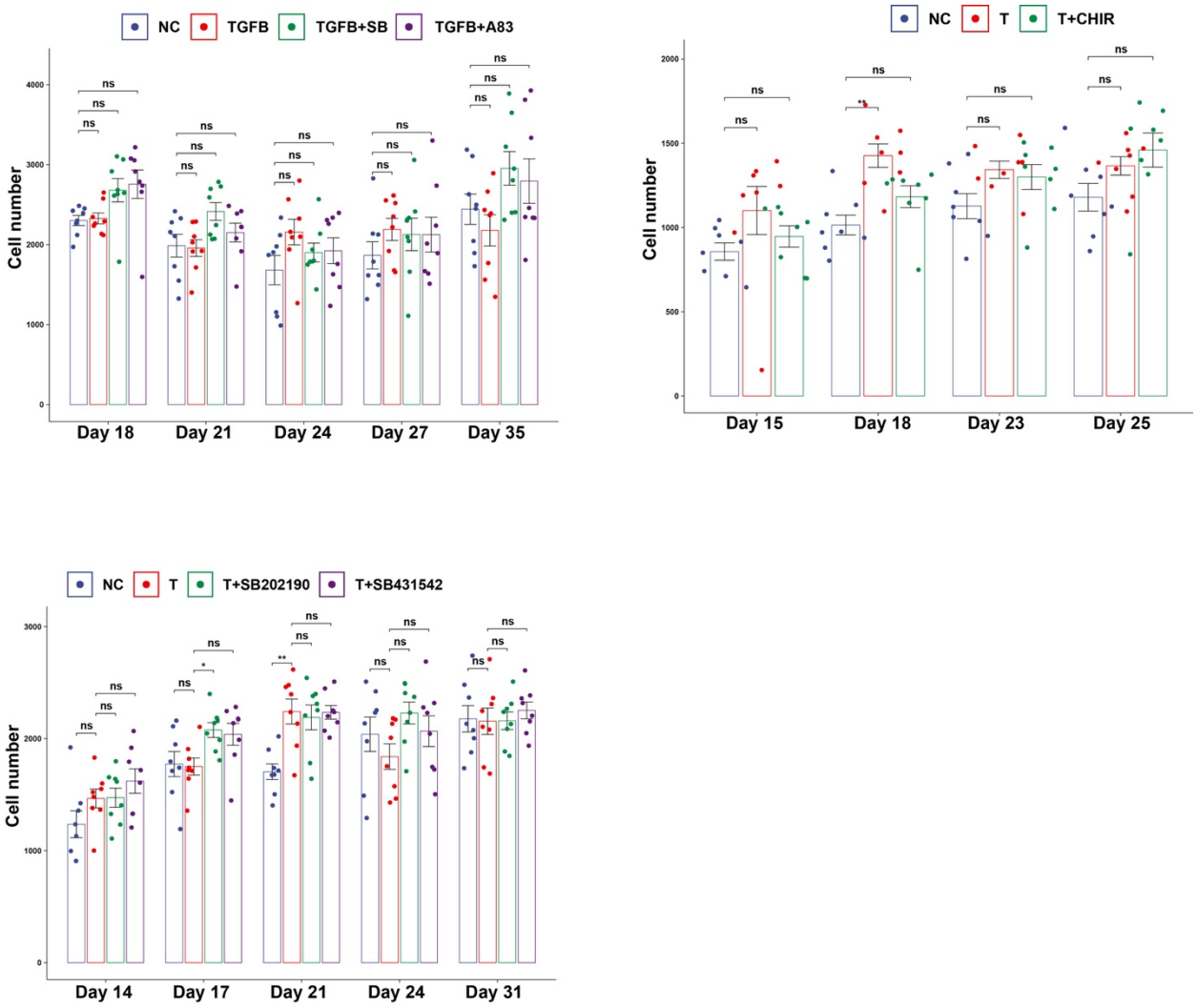

Figure S9. microHO viability was not affected by addition of 50 ng/ml TGFβ1 (T) or 10 uM of the TGFRβ1 (SB431542) or p38 α (SB202190) inhibitor. microHOs were prepared and incubated with no addition (NC), TGFβ1 (T), or TGFβ1 ± the indicated inhibitor on day 13. The number of cells in each microHO was measured by counting the number of nuclei (stained with Hoechst 33342) on days 14 to 31. Each bar is the average of 8 individual measurements ± the SE, and individual datapoints are shown as dots. Analyses of the number of cells in microHO cultures after addition of TGFβ1 ± inhibitors revealed that these additions did not cause a significantly change (ns) in number of cells in treated microHOs.

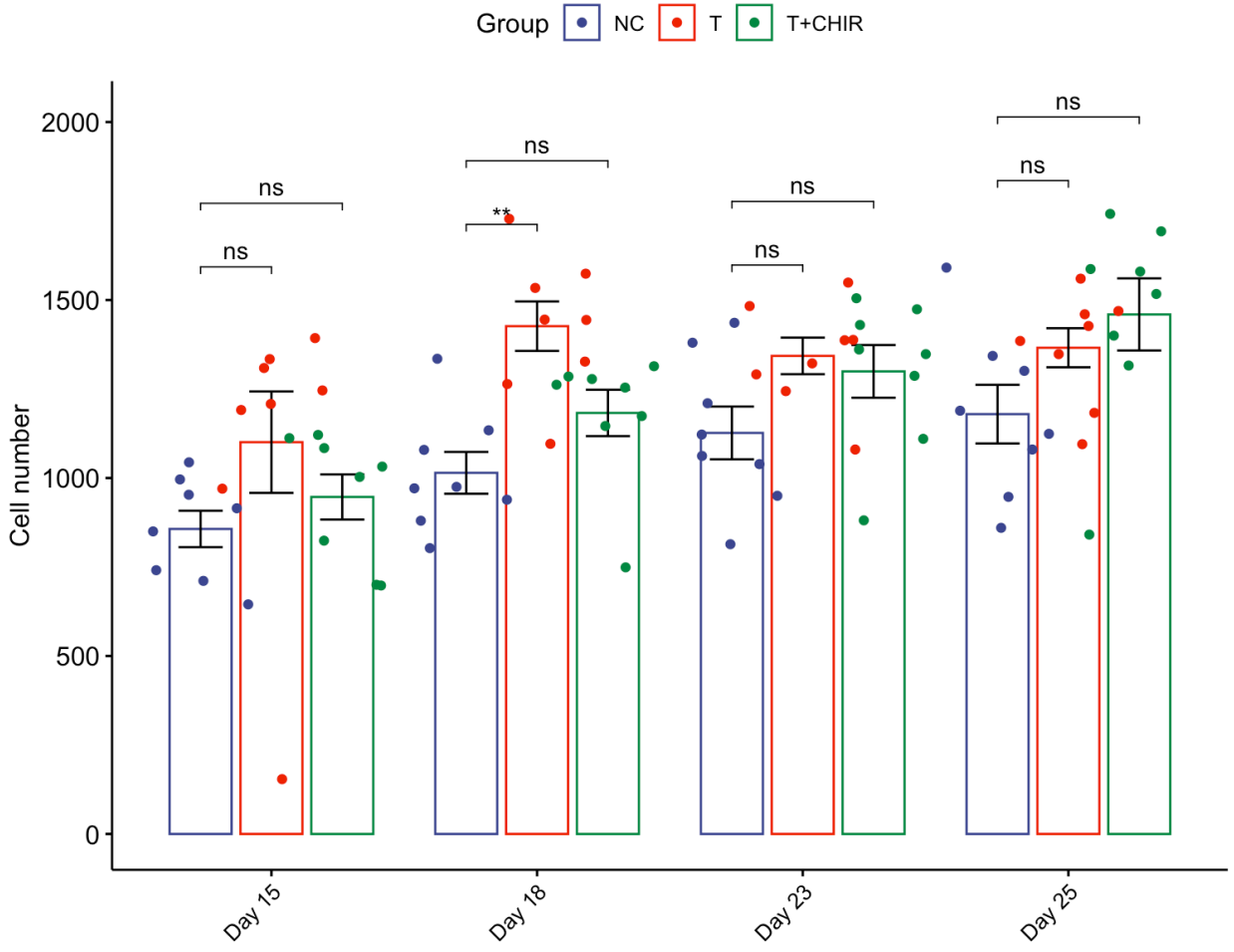

Figure S10. The addition of 50 ng/ml TGFβ1 and 10 uM CHIR99021 to microHO cultures did not alter microHO viability. microHOs were prepared and incubated with no addition (NC), TGFβ1 (T), or TGFβ1 + 10 uM CHIR99021 on day 13. The number of cells in each microHO was measured by counting the number of nuclei (stained with Hoechst 33342) on days 15 to 25. Each bar is the average of 8 individual measurements ± the SE. The number of cells in the microHO cultures after addition of TGFβ1 or CHIR99021 was not significantly altered (ns) relative to that of the control microHOs.

Table S3. Twenty mRNAs that are differentially expressed in each of the 14 cell clusters identified in microHOs. The gene symbol, p-value, adjusted p-value, and fold differential expression (log_2) for each differentially expressed gene are shown. Pct.1 and Pct.2 indicates the contribution of that feature to defining the indicated cluster based upon principal component analysis.

Cluster	*Gene*	P-val	avg_log2(FC)	Pct.1	Pct.2	Adj P-val
0	*TIMP1*	0	2.65	0.92	0.47	0
0	*LTBP2*	0	2.12	0.91	0.26	0
0	*SCG2*	0	2.10	0.72	0.13	0
0	*SERPINE2*	0	1.98	0.98	0.71	0
0	*FN1*	0	1.96	1.00	0.99	0
0	*SERPINE1*	0	1.83	0.88	0.36	0
0	*TIMP3*	0	1.83	0.77	0.43	0
0	*RUNX1*	0	1.82	0.95	0.43	0
0	*UBASH3B*	0	1.81	0.80	0.24	0
0	*LINC00607*	0	1.70	0.59	0.16	0
0	*HMGB1*	0	1.67	0.99	0.83	0
0	*AC099489.1*	0	1.65	0.83	0.33	0
0	*NTM*	0	1.64	0.53	0.14	0
0	*LAMA2*	0	1.64	0.73	0.21	0
0	*HS3ST3A1*	0	1.63	0.79	0.30	0
0	*COL6A3*	0	1.61	0.96	0.61	0
0	*LNCAROD*	0	1.60	0.45	0.06	0
0	*MICAL2*	0	1.53	0.93	0.55	0
0	*AC015522.1*	0	1.51	0.87	0.54	0
0	*FAP*	0	1.50	0.60	0.08	0
1	*PLIN2*	0	1.54	0.87	0.63	0
1	*IL1RL1*	1.46E-182	1.42	0.55	0.27	5.24E-178
1	*MME*	1.60E-274	1.36	0.88	0.65	5.72E-270
1	*AL118558.1*	2.97E-186	1.23	0.54	0.26	1.07E-181
1	*NFKB1*	2.43E-38	1.17	0.48	0.41	8.71E-34
1	*NID1*	6.35E-117	1.08	0.80	0.73	2.28E-112
1	*BAG3*	1.78E-279	1.07	0.88	0.65	6.40E-275
1	*HSPH1*	0	1.06	0.97	0.72	0
1	*DNAJB1*	6.73E-273	1.02	0.95	0.75	2.41E-268

1	*ELOVL5*	2.87E-166	1.01	0.81	0.70	1.03E-161
1	*EPAS1*	5.91E-121	0.97	0.68	0.50	2.12E-116
1	*IL18R1*	6.26E-147	0.97	0.69	0.48	2.25E-142
1	*NCOA7*	5.45E-118	0.97	0.73	0.61	1.95E-113
1	*NEAT1*	2.51E-252	0.97	0.99	0.97	9.00E-248
1	*DLK1*	1.16E-235	0.95	0.94	0.70	4.15E-231
1	*NAMPT*	3.97E-110	0.93	0.64	0.51	1.42E-105
1	*HIVEP2*	1.60E-178	0.93	0.87	0.73	5.74E-174
1	*IGF2*	5.24E-232	0.93	1.00	1.00	1.88E-227
1	*MIR4435-2HG*	1.56E-131	0.92	0.87	0.76	5.61E-127
1	*EPS8*	1.90E-156	0.92	0.87	0.76	6.81E-152
2	*AFP*	0	4.93	0.80	0.20	0
2	*THRB*	0	3.53	0.93	0.27	0
2	*CDH12*	0	3.41	0.62	0.08	0
2	*FGB*	0	3.33	0.71	0.04	0
2	*APOB*	0	2.91	0.50	0.06	0
2	*SNTB1*	0	2.83	0.87	0.10	0
2	*MECOM*	0	2.75	0.89	0.31	0
2	*UNC13C*	0	2.72	0.87	0.20	0
2	*LINC00511*	0	2.40	0.88	0.29	0
2	*KHDRBS2*	0	2.39	0.85	0.23	0
2	*CKB*	0	2.29	0.82	0.18	0
2	*NEDD4L*	0	2.26	0.97	0.57	0
2	*CCSER1*	0	2.18	0.94	0.38	0
2	*CFTR*	0	2.13	0.66	0.05	0
2	*MACC1*	0	2.09	0.81	0.07	0
2	*TTC6*	0	2.04	0.81	0.10	0
2	*CHST9*	0	2.04	0.86	0.18	0
2	*CDH17*	0	2.03	0.62	0.02	0
2	*PRDM1*	0	2.02	0.62	0.03	0
2	*PARD3B*	0	2.00	0.85	0.35	0
3	*SIPA1L2*	1.05E-283	1.69	0.96	0.81	3.77E-279
3	*CHRM2*	1.08E-248	1.65	0.74	0.35	3.89E-244
3	*RYR2*	9.46E-230	1.64	0.79	0.40	3.39E-225
3	*RNF150*	9.67E-155	1.50	0.67	0.40	3.47E-150
3	*CNTN5*	6.20E-144	1.45	0.51	0.22	2.22E-139
3	*ADAMTS9*	2.21E-218	1.44	0.90	0.66	7.94E-214
3	*TMEM132C*	1.25E-219	1.34	0.86	0.52	4.49E-215

3	*PDE10A*	6.37E-73	1.26	0.74	0.65	2.28E-68
3	*EPHA3*	5.51E-218	1.22	0.43	0.12	1.98E-213
3	*PCDH17*	3.08E-186	1.22	0.70	0.36	1.10E-181
3	*CPED1*	1.84E-171	1.22	0.83	0.57	6.58E-167
3	*KCTD8*	2.17E-108	1.18	0.64	0.40	7.77E-104
3	*CCBE1*	1.95E-204	1.17	0.48	0.15	7.01E-200
3	*LINC01192*	3.31E-251	1.17	0.40	0.09	1.19E-246
3	*PLXDC2*	9.37E-148	1.12	0.88	0.70	3.36E-143
3	*CERS6*	6.37E-252	1.11	0.97	0.91	2.28E-247
3	*HHIP*	4.75E-117	1.11	0.40	0.16	1.71E-112
3	*IL1RL1*	3.91E-138	1.11	0.59	0.28	1.40E-133
3	*TSHZ2*	1.41E-80	1.09	0.78	0.62	5.04E-76
3	*LINC01088*	5.14E-97	1.08	0.47	0.24	1.84E-92
4	*PDZRN4*	0	2.89	0.88	0.26	0
4	*FGFR2*	0	2.49	0.97	0.34	0
4	*PWRN1*	0	2.47	0.93	0.38	0
4	*FREM1*	0	2.40	0.98	0.57	0
4	*RSPO2*	0	2.29	0.73	0.19	0
4	*IGFBP3*	0	2.24	0.99	0.71	0
4	*TGFBR3*	0	2.19	1.00	0.61	0
4	*RELN*	0	2.13	0.97	0.38	0
4	*ADAM12*	0	2.00	0.96	0.51	0
4	*GREM2*	0	1.94	0.84	0.30	0
4	*KCNIP4*	0	1.93	0.95	0.44	0
4	*LDB2*	0	1.93	0.99	0.57	0
4	*CXCL14*	0	1.83	0.73	0.17	0
4	*LRRTM4*	2.04E-304	1.79	0.81	0.35	7.33E-300
4	*ITGA8*	0	1.79	0.96	0.42	0
4	*VEGFC*	0	1.78	0.79	0.26	0
4	*EPHA7*	0	1.77	0.96	0.60	0
4	*DPP10*	0	1.74	0.82	0.32	0
4	*PLXNA4*	0	1.73	0.75	0.24	0
4	*TEK*	0	1.70	0.97	0.36	0
5	*HAPLN1*	0	2.86	0.95	0.23	0
5	*CDH13*	0	2.14	0.97	0.36	0
5	*KCNIP4*	0	1.97	0.93	0.45	0
5	*CRHBP*	0	1.96	0.63	0.14	0
5	*KCNQ5*	0	1.87	0.95	0.38	0
5	*TNC*	0	1.79	0.87	0.32	0

5	*MASP1*	0	1.67	0.90	0.37	0
5	*VIM*	0	1.66	1.00	0.81	0
5	*AL365295.1*	2.58E-254	1.60	0.76	0.32	9.26E-250
5	*MEST*	0	1.58	0.96	0.56	0
5	*IGDCC3*	0	1.57	0.92	0.37	0
5	*EDIL3*	0	1.56	0.98	0.64	0
5	*DOK4*	0	1.56	0.90	0.30	0
5	*PRTG*	0	1.55	0.97	0.54	0
5	*NRP1*	1.23E-290	1.49	0.96	0.59	4.43E-286
5	*KDR*	0	1.47	0.95	0.52	0
5	*ITGA8*	0	1.47	0.95	0.43	0
5	*NID2*	0	1.44	0.98	0.56	0
5	*FLT1*	7.60E-229	1.44	0.98	0.70	2.73E-224
5	*ADAMTS12*	0	1.43	0.94	0.45	0
6	*TOP2A*	0	2.22	0.95	0.15	0
6	*DIAPH3*	0	2.20	0.98	0.22	0
6	*PDZRN4*	0	2.19	0.90	0.29	0
6	*MIR924HG*	0	2.13	0.69	0.14	0
6	*ASPM*	0	2.07	0.94	0.16	0
6	*CENPF*	0	2.06	0.93	0.17	0
6	*MKI67*	0	1.95	0.91	0.13	0
6	*TPX2*	0	1.91	0.94	0.19	0
6	*RFC3*	0	1.89	0.96	0.25	0
6	*FGFR2*	0	1.87	0.98	0.36	0
6	*RELN*	0	1.80	0.98	0.40	0
6	*ARHGAP6*	4.54E-237	1.78	0.95	0.49	1.63E-232
6	*HS3ST4*	8.03E-56	1.78	0.59	0.34	2.88E-51
6	*PWRN1*	3.10E-275	1.72	0.94	0.40	1.11E-270
6	*ITGA8*	1.62E-259	1.65	0.98	0.44	5.81E-255
6	*APOLD1*	1.15E-303	1.65	0.87	0.31	4.13E-299
6	*FREM1*	9.11E-249	1.65	0.99	0.58	3.27E-244
6	*TGFBR3*	4.85E-265	1.60	0.99	0.63	1.74E-260
6	*CIT*	0	1.57	0.90	0.12	0
6	*AP001347.1*	0	1.57	0.97	0.32	0
7	*TOP2A*	0	2.50	0.96	0.15	0
7	*MKI67*	0	2.46	0.97	0.13	0
7	*HAPLN1*	0	2.41	0.94	0.25	0
7	*DIAPH3*	0	2.39	0.97	0.22	0

7	*CENPF*	0	2.38	0.95	0.17	0
7	*TPX2*	0	2.16	0.96	0.19	0
7	*ASPM*	0	1.90	0.94	0.16	0
7	*CIT*	0	1.79	0.89	0.12	0
7	*RFC3*	0	1.79	0.93	0.26	0
7	*CRHBP*	2.42E-271	1.78	0.69	0.15	8.67E-267
7	*CDH13*	1.76E-252	1.77	0.94	0.38	6.32E-248
7	*CENPE*	0	1.73	0.92	0.31	0
7	*BUB1*	0	1.72	0.89	0.12	0
7	*MIR924HG*	9.30E-288	1.68	0.68	0.15	3.34E-283
7	*KIF14*	0	1.61	0.86	0.13	0
7	*RRM2*	0	1.59	0.89	0.12	0
7	*MIS18BP1*	1.69E-271	1.56	0.92	0.39	6.05E-267
7	*SMC4*	1.95E-290	1.56	0.97	0.55	6.99E-286
7	*ANLN*	0	1.55	0.90	0.20	0
7	*MEST*	1.35E-208	1.53	0.97	0.58	4.85E-204
8	*NTN4*	0	3.50	0.81	0.10	0
8	*LINC00511*	0	3.12	0.98	0.33	0
8	*NRG3*	1.15E-164	3.09	0.91	0.52	4.13E-160
8	*SERPINA1*	0	2.61	0.65	0.10	0
8	*DTNA*	7.26E-263	2.58	0.90	0.31	2.60E-258
8	*LINC01239*	0	2.38	0.72	0.09	0
8	*MAP2*	0	2.32	0.67	0.09	0
8	*AC005062.1*	0	2.29	0.70	0.08	0
8	*ITGA2*	3.23E-250	2.28	0.90	0.29	1.16E-245
8	*CDH6*	0	2.26	0.82	0.15	0
8	*ITGB6*	0	2.10	0.71	0.09	0
8	*MACC1*	0	2.06	0.83	0.12	0
8	*CASC15*	1.07E-211	2.06	0.96	0.44	3.83E-207
8	*PDE5A*	5.96E-142	2.00	0.75	0.28	2.14E-137
8	*FRMD5*	8.76E-235	1.93	0.74	0.18	3.14E-230
8	*CPA6*	0	1.89	0.53	0.02	0
8	*CYP1B1*	3.75E-244	1.82	0.73	0.16	1.34E-239
8	*SPP1*	8.38E-135	1.79	0.33	0.05	3.00E-130
8	*CCSER1*	2.67E-192	1.79	0.96	0.42	9.58E-188
8	*LAMC2*	6.04E-220	1.78	0.72	0.17	2.17E-215
9	*CTNND2*	1.19E-300	3.32	0.94	0.28	4.28E-296
9	*CDH6*	0	2.98	0.91	0.15	0

9	*ONECUT2*	0	2.82	0.86	0.08	0
9	*ROBO2*	4.51E-200	2.82	0.99	0.73	1.62E-195
9	*DACH1*	5.21E-294	2.79	0.88	0.22	1.87E-289
9	*UNC5D*	0	2.77	0.92	0.21	0
9	*ONECUT1*	0	2.77	0.89	0.05	0
9	*PDE3A*	1.15E-152	2.73	0.91	0.57	4.13E-148
9	*CUX2*	0	2.70	0.59	0.01	0
9	*GUCY1A2*	1.96E-216	2.70	0.85	0.27	7.05E-212
9	*CHST9*	0	2.63	0.94	0.23	0
9	*DCDC2*	0	2.60	0.75	0.06	0
9	*CTNNA2*	0	2.51	0.53	0.04	0
9	*SHANK2*	0	2.51	0.96	0.24	0
9	*ERBB4*	1.64E-244	2.34	0.86	0.23	5.90E-240
9	*LRRC7*	0	2.33	0.58	0.06	0
9	*FRAS1*	2.30E-186	2.33	0.99	0.61	8.24E-182
9	*SERPINA1*	0	2.24	0.74	0.09	0
9	*SLC4A4*	2.26E-106	2.23	0.81	0.46	8.12E-102
9	*KHDRBS2*	2.60E-229	2.23	0.91	0.27	9.33E-225
10	*AC099520.1*	0	2.94	0.48	0.04	0
10	*GABRB3*	2.29E-105	2.83	0.29	0.04	8.21E-101
10	*PI16*	0	2.53	0.69	0.03	0
10	*ADAMTS17*	2.76E-79	2.25	0.50	0.17	9.91E-75
10	*SNTG2*	6.56E-250	2.14	0.51	0.06	2.35E-245
10	*CD55*	1.27E-207	2.09	0.83	0.24	4.54E-203
10	*ZBTB7C*	9.01E-294	2.09	0.63	0.08	3.23E-289
10	*MIAT*	0	2.00	0.76	0.12	0
10	*HTRA3*	1.58E-132	1.88	0.67	0.21	5.67E-128
10	*IGFBP6*	0	1.83	0.67	0.09	0
10	*KLF3*	2.02E-111	1.71	0.89	0.55	7.24E-107
10	*TMEM132D*	3.58E-122	1.66	0.41	0.07	1.28E-117
10	*C3*	1.14E-49	1.65	0.45	0.18	4.10E-45
10	*CPAMD8*	1.20E-160	1.61	0.73	0.21	4.30E-156
10	*SORCS2*	4.69E-123	1.59	0.72	0.26	1.68E-118
10	*ATP10A*	1.23E-238	1.58	0.63	0.10	4.42E-234
10	*PODXL*	6.72E-88	1.57	0.55	0.18	2.41E-83
10	*AC020637.1*	2.02E-95	1.56	0.28	0.04	7.23E-91
10	*PRDM16*	5.10E-108	1.53	0.61	0.18	1.83E-103
10	*NEAT1*	1.38E-80	1.52	0.99	0.97	4.94E-76

11	*KCNMA1*	2.72E-204	2.68	0.96	0.33	9.75E-200
11	*LINC02388*	4.68E-142	2.59	0.62	0.14	1.68E-137
11	*PKHD1L1*	0	2.48	0.69	0.02	0
11	*PDE1C*	1.33E-81	2.37	0.47	0.12	4.76E-77
11	*DIRC3*	1.97E-81	2.12	0.84	0.42	7.06E-77
11	*COBLL1*	5.53E-129	2.09	0.95	0.50	1.98E-124
11	*NPNT*	3.43E-142	1.97	0.92	0.39	1.23E-137
11	*CELF2*	9.44E-105	1.96	0.80	0.35	3.39E-100
11	*GREB1L*	1.54E-117	1.89	0.94	0.55	5.51E-113
11	*EZR*	2.61E-135	1.85	0.98	0.58	9.37E-131
11	*FKBP5*	1.38E-124	1.82	0.98	0.64	4.96E-120
11	*PODXL*	2.64E-127	1.82	0.68	0.18	9.46E-123
11	*IGFBP5*	3.15E-99	1.82	0.88	0.40	1.13E-94
11	*PLXDC2*	2.56E-76	1.81	0.96	0.71	9.19E-72
11	*ARAP2*	7.40E-113	1.80	0.83	0.33	2.65E-108
11	*CDH20*	9.13E-145	1.78	0.50	0.09	3.27E-140
11	*ARHGAP6*	1.42E-86	1.73	0.90	0.51	5.09E-82
11	*ZBTB16*	2.36E-102	1.72	0.84	0.37	8.46E-98
11	*PDPN*	2.60E-162	1.71	0.91	0.33	9.31E-158
11	*GALNT18*	3.98E-100	1.69	0.67	0.21	1.43E-95
12	*XACT*	6.48E-143	3.99	0.60	0.11	2.32E-138
12	*EMCN*	0	3.14	0.88	0.02	0
12	*CRHBP*	3.41E-243	3.11	0.90	0.16	1.22E-238
12	*CALCRL*	6.74E-210	3.09	0.99	0.30	2.42E-205
12	*FLI1*	1.80E-179	2.77	0.98	0.37	6.47E-175
12	*AL365295.1*	1.26E-55	2.55	0.69	0.34	4.51E-51
12	*KDR*	7.86E-116	2.37	0.96	0.55	2.82E-111
12	*LDB2*	2.05E-102	2.19	0.97	0.60	7.37E-98
12	*DYSF*	0	2.18	0.84	0.10	0
12	*RASGRP3*	0	2.17	0.81	0.05	0
12	*MEF2C*	7.47E-177	2.14	0.89	0.24	2.68E-172
12	*AC010737.1*	8.44E-210	2.13	0.81	0.15	3.03E-205
12	*HECW2*	1.26E-46	2.11	0.75	0.42	4.53E-42
12	*ZEB1*	1.19E-131	2.10	0.97	0.50	4.25E-127
12	*PRKCH*	6.22E-218	2.07	0.90	0.18	2.23E-213
12	*LIMCH1*	1.48E-147	2.04	0.94	0.31	5.32E-143
12	*ITGA9*	1.28E-128	2.00	0.88	0.31	4.59E-124
12	*NCKAP5*	3.89E-160	1.96	0.72	0.14	1.39E-155

12	*ST6GAL1*	3.28E-82	1.96	0.74	0.30	1.18E-77
12	*FAR2*	5.76E-246	1.95	0.74	0.10	2.06E-241
13	*TTN*	1.28E-42	2.66	0.94	0.23	4.58E-38
13	*PODXL*	4.56E-51	2.66	0.94	0.19	1.63E-46
13	*GLYATL2*	1.45E-45	2.56	0.88	0.18	5.21E-41
13	*FGF13*	2.77E-50	2.54	0.92	0.17	9.92E-46
13	*EPHA6*	5.71E-35	2.53	0.98	0.30	2.05E-30
13	*AC084816.1*	1.20E-36	2.46	0.77	0.16	4.32E-32
13	*HS6ST3*	3.82E-91	2.40	0.65	0.04	1.37E-86
13	*DOK6*	1.25E-42	2.33	0.98	0.26	4.50E-38
13	*PCAT14*	6.95E-45	2.29	0.88	0.18	2.49E-40
13	*FAM184A*	1.06E-60	2.22	0.96	0.17	3.80E-56
13	*GPC3*	2.84E-23	2.17	0.94	0.42	1.02E-18
13	*SLC2A3*	1.26E-23	2.11	0.96	0.54	4.54E-19
13	*NRCAM*	7.54E-44	2.06	0.88	0.18	2.70E-39
13	*CUBN*	1.97E-20	2.06	0.69	0.22	7.06E-16
13	*APOB*	2.10E-50	2.05	0.75	0.10	7.54E-46
13	*RASGEF1B*	4.37E-37	2.04	0.85	0.20	1.57E-32
13	*SLCO2A1*	1.56E-40	2.03	0.79	0.15	5.59E-36
13	*SYTL5*	4.42E-44	2.03	0.83	0.16	1.59E-39
13	*FREM2*	5.98E-34	1.96	1.00	0.35	2.15E-29
13	*ALK*	1.52E-10	1.93	0.38	0.10	5.47E-06